CENTRO DE INVESTIGACIONES EN OPTICA, A.C.

® **POSGRADO INTERINSTITUCIONAL EN CIENCIA Y TECNOLOGÍA**

TOWARDS THE CONSTRUCTION OF AN ELECTRIC GENERATOR FOR QUADROTORS: MODELING, DESIGN, AND CONTROL OF THE ELECTRONICS

TESIS

Versión definitiva. Incluye cambios sugeridos por revisores.

QUE PARA OBTENER EL GRADO
ACADÉMICO DE

MAESTRO EN CIENCIA Y TECNOLOGÍA
EN LA ESPECIALIDAD DE
MECATRÓNICA

PRESENTA

ING. RODOLFO ISAAC VERDÍN MONZÓN

Visto bueno
01 de marzo de 2022

Gerardo Flores
Director de tesis

DIRECTOR DE TESIS
DR. GERARDO RAMÓN FLORES COLUNGA

LEÓN, GUANAJUATO, MARZO, 2022.

POSGRADO INTERINSTITUCIONAL

Towards the construction of an electric generator for quadrotors: modeling, design, and control of the electronics

Acknowledgements

I would like to show my gratitude to Consejo Nacional de Ciencia y Tecnología (CONACYT) who brought me a Master scholarship, that was determinant in the development and continuity of my project. I also want to thank the Academic authorities of Centro de Investigaciones en Óptica (CIO). Similarly I am very thankful with my advisor, Dr. Gerardo Flores, for his continuous support.

To my parents and brother for being supports in my life, and God for giving me these years of life.

Publications

Conference papers

- Teleoperated aerial manipulator and its avatar. Communication, system's interconnection, and virtual world. **Rodolfo Verdín**, Germán Ramírez, Carlos Rivera, Gerardo Flores. International Conference on Unmanned Aircraft Systems 2021 (ACCEPTED).

Journal papers

- Robust and adaptive controllers for the three-phase AC/DC converter **Rodolfo Verdín**, Gerardo Flores. IEEE/CAA journal of automatica Sinica (SUBMITTED).

Abstract

This thesis develops the basis for the design and construction of a power generation system for application in unmanned aerial vehicles (UAV) with quadrotor structure. This system is integrated by a power generation stage, with two-stroke internal combustion engine of two Horse-Power (HP) coupled with a brushless Altern Current (AC) motor. In particular we will focus more on the second stage that is rectification and voltage regulation. In this work a three-phase controlled rectifier is proposed, modeled, and simulated for this purpose a robust adaptive control is implemented to regulate the output voltage or current and to adapt even when the output load is unknown or changes. The mathematical model was worked in $d-q$ space and the controller was designed considering this model in which the states i_d (direct current) i_q (reactive current) and v_o (system output voltage) are controlled.

Contents

List of Tables

List of Figures

CHAPTER 1

Introduction

Developments in the control systems of unmanned aerial vehicles (UAVs) have made them more robust and maneuverable, which has made possible their progressive introduction into the daily and working life of society. Similarly, the advance of Artificial inteligence (AI), Simultaneous mapping and localization (SLAM), and robotics in general, has made possible the search for applications in diferents fields for example social, agricultural and industrial, so these vehicles have been increasingly introduced. One of the first limitation in UAV's especially multirotors is the flight time autonomy, having an average of fifteen - twenty minutes depending on flight conditions, vehicle weight, payload and environmental conditions. To solve this problem several strategies have been proposed to make UAV's flights more efficient in specific tasks. Within this work, the construction of a modular electric mini-generator is proposed as an option for quadrotors. This project is very broad and complex due to the different systems that integrate it. Therefore, we will limit ourselves to a specific problem without abandoning the construction of a prototype and performing basic tests of electrical generation. In this work preference is given to the three-phase rectification stage, a robust adaptive control is proposed and designed for voltage regulation of a controlled three-phase rectifier.

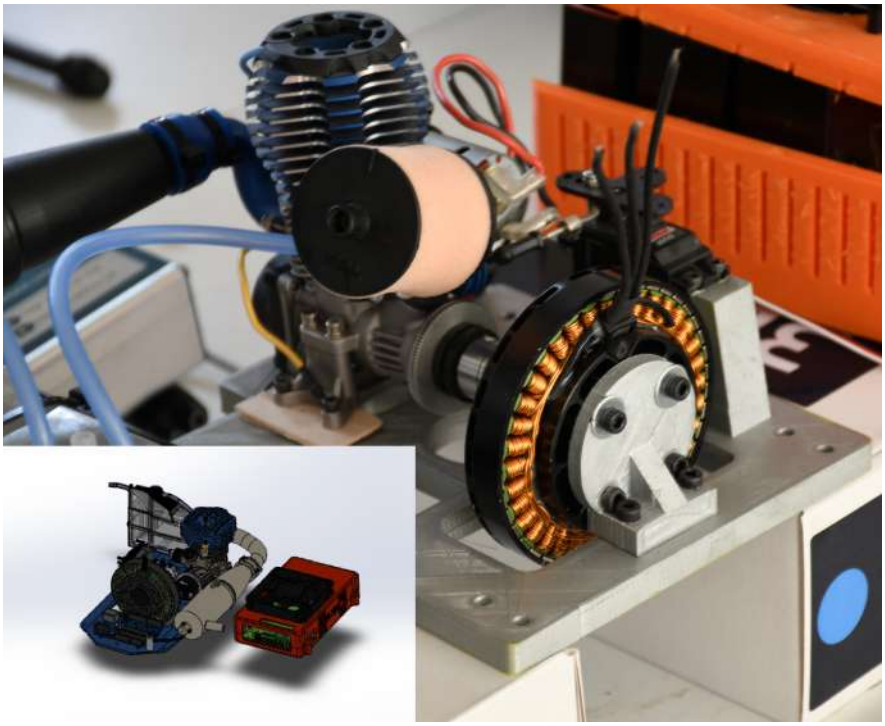

Figure 1.1: First prototype of a modular three-phase mini-generator for quadrotor applications.

This thesis is organized in the following sections: In Chapter 1 different studies related to UAV time-of-flight solutions are presented, the problem is stated as well as the objectives and justification of the project. In the Chapter 2, the state of the art corresponding to the specific problem to be solved is presented. In Chapter 3 the whole theory for the control of the proposed three-phase rectifier is developed, whose objective is the regulation of voltage and current and to achieve a reactive current equal to zero, which allows maintaining power factors close to one. Chapter 4 presents the performed experiments and their results, first, the comparison of three controllers which are simulated is presented. Later a SITL (Software in the loop) simulation of the adaptive robust rectifier and its results are presented. Subsection 4.2.1 presents the progress currently being made in the construction of the generator. Finally, in the Section 5 the conclusions of this work are presented as well as the future works and scope that this work could have.

1.1 Background

1.1.1 Hybrid UAVs

Hybrid or flight transition vehicles are vehicles that integrate the flight characteristics of a multirotor and those of an airplane. In this way, it is possible to have vertical take-off and to move horizontally [1]. The orientation of this depends on the speed of each of its engines, these vehicles are robust to withstand external loads, have good stability and travel long distances in a short time. Fixed-wing UAVs commonly known as airplanes have an engine at the front for propulsion and a rudder to steer the vehicle. One of their advantages is that they can travel long distances in a very short time. The disadvantage is that they cannot remain in a fixed position and must always be in motion. Multirotors have the characteristic of taking off in a short space, fixing and maintaining their position at one point and rotating on their axis [2] [3]. The drawback is that they are vehicles that consume too much energy due to the number of motors in them. VTOLs, tiltrotors and tail-sitter, are hybrid UAVs that contain both features in the Figure (1.2) shown are two examples of vehicles with hybrid flight mode, which are used in various tasks. This vehicles reduce the disadvantages they have separately. Even so, the flight time is the same. In the following sections we analyze alternatives on vehicles that improve performance and flight time, increasing the productivity with the use of UAVs.

In the case of VTOL aircraft, the advantages are a smaller launch and recovery area, rapid deployment and translation capabilities. Each of these capabilities makes this aircraft an optimal choice for certain sectors, such as precision agriculture [4], emergency response and transportation [5]. For example, the ability to launch an aircraft vertically and without the need for a runway makes these aircraft incredibly attractive to farmers. For example collect aerial imagery without the burden of launching a manned aircraft that often requires a runway. For those working in emergency response, the ability to quickly deploy an aircraft is essential. VTOL aircraft easily meet this need. They can quickly deploy to hazardous areas that may be difficult for humans to access. The final advantage of VTOL aircraft lies in their translational flight capability. They can easily move quickly, slowly, longitudi-

nally and laterally. Although these vehicles show advantages, the flight limitation remains a problem to be solved. The future of VTOL drones is largely driven by innovative technologies. Advances in robotics, remote sensing, and aviation sustainability have directly contributed to improvements in the design and operation of these aircraft. What were once considered limitations are now technological breakthroughs.

(a) Tail sitter UAV used in various tasks, especially in precision agriculture [6].

(b) VTOL ”Sierra” is used for border surveillance, infrastructure inspection, naval operations, reference tracking [7].

Figure 1.2: UAVs with hybrid flight modes, these are used when long distances are required in a short time, since it has the characteristics of a multirotor it can maintain position.

The disadvantages of the VTOL aircraft platform include energy efficiency, airspeed limitations, and lower operating altitude capabilities. Given the recent emphasis on aviation and aircraft sustainability, energy efficiency ratings are a key consideration not only for VTOL aircraft but for all platforms [8].

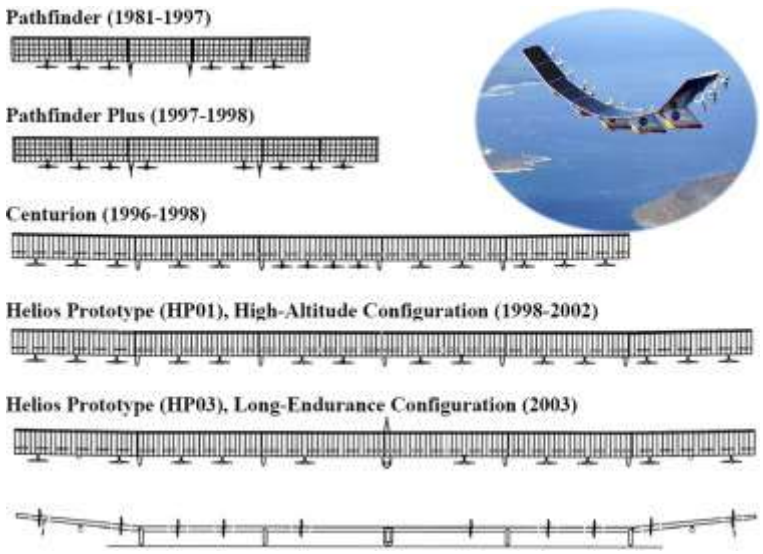

Figure 1.3: The evolution of solar airplanes in the ERAST project [12].

1.1.2 Solar energy

On the other hand, there are also alternatives where the main source of energy is solar energy obtained through photovoltaic cells, that transform photons into electrical energy from the photoelectric effect [9]. The conversion efficiency of photovoltaic modules will depend directly on the type of photovoltaic cells used. Commercially available solar cells have conversion efficiencies ranging from 14% to 22% [10]. Monocrystalline silicon cells have higher conversion efficiencies than amorphous or polycrystalline cells, but are more expensive due to their wafer structure; they are also more fragile. Amorphous or thin-film solar cells are lighter and have a higher resistance to bending. They allow simple implementations on curved surfaces and have the lowest conversion efficiency range of 6 to 14% [11].

Due to the power generated over square meter ratio they are commonly implemented in low-power fixed-wing vehicles. The level flight power requirement of solar-powered aircraft has a cubic relationship to level flight speed. Solar-powered aircraft typically fly at relatively low speed to compensate for gravity, solar-powered aircraft should have a higher lift coefficient than conventional aircraft. As this ratio is the power generated concerning the size of the solar cell, in general large solar cells are used for the required power. But the cells must also be capable of supplying the power required to lift the vehicle for

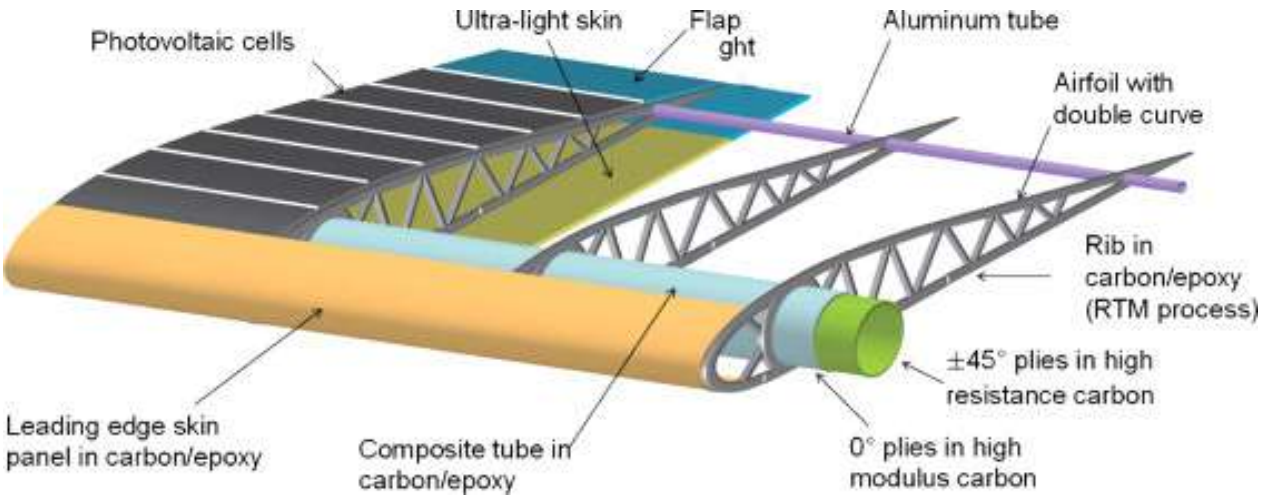

Figure 1.4: A typical wing structure with solar cells [13]

this same reason, the UAVs currently known that use solar energy as a source are fixed-wing vehicles and as can be seen in the Figure (1.5a) are peculiar designs in which the sustainability of the vehicle is exploited as much as possible by taking advantage of the gusts.

In the design of vehicles, the cell itself is considered as part of the wing structure, which means that the cell is made in the shape of the wing so that cells with larger dimensions can be used to capture solar energy [14] [15]. Flights in the atmosphere depend only on solar radiation, as its main source of energy and the amount of energy produced depends on factors such as the geographical location of the vehicle, the orientation of the solar photovoltaic array concerning the sun, and the local meteorological condition. For this reason, research on these aircraft focuses on wing design [16] to capture the maximum amount of lightning regardless of orientation As shown in the Figure (1.4), and energy management methods are used to allow the unused charge to be stored for when the system requires it, and route planning is used to efficiently plot routes that require the least possible energy expenditure. The research of these vehicles is aimed at reducing the dimensions of the solar modules, to reduce the weight.

As in the previous point, academic but not commercial VTOL prototypes have been developed integrating solar cells [17] [18]. This research although very recent is interesting since they have controls that modify the morphology of the wing adapting to the orientation

in which the sun is located as shown in the Figure (1.5b). As in airplanes, the structure is built with the same solar cell. So they have the advantage of taking off and sustaining the flight vertically and traveling long distances for a long time as long as there is enough energy.

(a) The test flight of the Sky-sailor [19].

(b) Tail sitter powered with solar energy [18].

(c) Solar-powered Sentera quadrotor, these quadrotors still have limitations, because the cells must supply the power needed for the four engines at takeoff [20]

Figure 1.5: Different configurations of UAVs are powered by solar energy, fixed-wing vehicles are the most efficient using this alternative, while multi-rotors require more power due to the number of motors that must always sustain their flight.

In the quadrotors, the challenge becomes more interesting due to the number of motors available, more motors mean more energy expenditure. For this reason, more efficient cells and a larger frame must be selected. The size of the quadrotor UAV is also influenced by the allowable operating irradiance and temperature conditions. Designing for low irradiance conditions results in large size and high-cost UAVs, but generates excess energy during high irradiance cycles. Small-scale solar quadrotors have been developed

as shown in Figure (1.5c). In the work of [20] and [21] who have a quadrotor that requires a power of 1KW (Kilowatts) which is a lower power than that required in this work.

1.1.3 Hydrogen cells

Recently fuel cell-based power system for unmanned aerial vehicles has become a hot research topic in the aviation industry and academia [22] [23]. The most mature and commercially available lightweight fuel cell systems for UAV applications are proton exchange membrane (PEM) fuel cells [24] powered by compressed hydrogen. In a hybrid fuel cell system (FCHS) [25] the fuel cell is the primary power source and the battery is the secondary power source. Ideally, the fuel cell provides continuous power and the battery gives the system a better response to dynamic loads. Response to dynamic loads provides redundancy and serves as a power reserve for emergency landings. The subsystems of a hybrid fuel cell system are fuel cell, balance of plant (BoP), hybrid battery and hydrogen storage. The balance of plants includes the control electronics, thermal and moisture management systems, etc in the Figure (1.6a) can see an example hybrid fuell sistem used in quadrotors while the Figure (1.6b) shows only the hydrogen cell module. The fuel cell configuration determines the power rating. The system has a certain empty weight and it is the hydrogen storage, the hybrid battery that determine the amount of energy in the system. A significant difference between a hybrid fuel cell system for fixed-wing UAVs and multirotor drones is the fuel cell and battery or the degree of hybridization. In general, fixed-wing UAVs have a relatively low and constant cruise power demand. The fuel cell is sized to match that power consumption, reducing the role of the hybrid battery to provide primary power for climb and maneuvering. Thus, the fuel cell can operate in much more ideal conditions and have a smaller and lighter hybrid battery. The energy demand of multirotor drones is typically higher than fixed-wing drones and the load profile is more dynamic [26]. Therefore, fuel cells must have a higher power rating and have a more active hybrid management system with a larger battery component. This increases the mass of the power system and introduces some additional challenges.

(a) Quadrotor using a fuel cell system, as a substitute for batteries, is integrated by, fuel cell, the balance of Plant (BoP), hybrid battery, hydrogen Storage [27].

(b) 2.4kW Fuel Cell Power Modules for drones, Intelligent energy [27].

Figure 1.6: Intelligent Energy is a fuel cell engineering company focused on the development and commercialization of its PEM fuel cell technologies for a variety of markets including automotive, stationary power, and unmanned aerial vehicles.

1.1.4 Fuel engine

Another alternative that has been working is the use of combustion engines as a power source for the vehicle, this alternative is not very new since the first vehicles that were considered UAVs had a combustion engine controlled autonomously or semi-autonomously. It is very common to find UAVs with aircraft configuration using combustion engines [28] [29], these are used in security tasks, mapping and study of minerals grounds or high risk for the population. But it is not common and neither has been studied in depth the use in multi-rotors. As mentioned UAVs with airplane configurations require only one engine to propel themselves, adding that the energy expenditure is much lower because they glide with the help of the wings that integrate it. So these vehicles only require control on a single-engine, but to advance in pitch can be integrated propellers that vary the angle of attack.

There are more advanced UAVs in which a generator transforms the mechanical energy transmitted from the combustion engine to electricity [30] is integrated, energy is stored to power the entire electrical system of the vehicle. During a certain time it works by fuel, in this flight stretch the generator will charge the batteries that later through a mechanism will make the change so that it functions by an electric motor, this gives more flight time. For example, as shown in the Figure (1.7) can be made VTOLs vehicles which during the

cruise flight mode using the combustion engine but during this stage [31] [32], the engine will also be able to generate electricity and then store it to power the four brushless motors which serve for the hover flight mode. Adding the characteristics of these vehicles now with a greater flight capacity we have vehicles that can travel long distances and have longer flight time.

(a) Flydragon company's commercial hybrid VTOL [32].

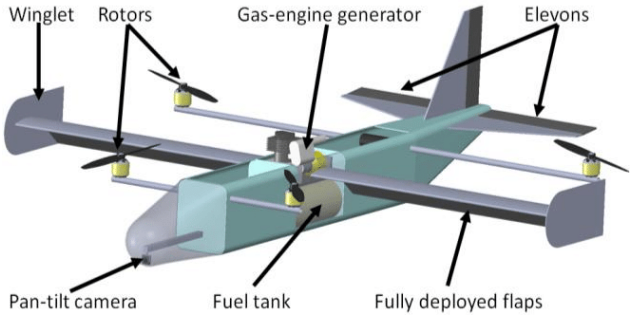

(b) Academic prototype of VTOL with electric generator [32].

Figure 1.7: This configuration of VTOL allows to propel with the combustion engine, and the same time allows to generate energy for the brushless motors, these have a mechanism that decouples the combustion engine and now acts as a brushless motor.

As in airplanes, there are two alternatives: using a single combustion engine to propel the vehicle or replacing the batteries with a mini generator that distributes power to the four electric motors.

Let's start with the first configuration. In articles [33] [34] a only combustion system is integrated in a quadrotor that have a mechanism with a series of pulleys that will distribute the movement to four propellers in the Figure (1.8a) can be visualized in a better way. But now something that distinguishes common quadrotors is that the trust and pitch, as well as the stability of the vehicle to disturbances is given by the revolutions that each engine will have. Giving a simple example if we move in trust required that all engines carry similar revolutions if we move in pitch the rear engines will give more revolutions than the front ones. In the quadrotors with a combustion engine, this does not exist to move in pitch only needs the combustion engine of sufficient power to generate a thrust if it is required to be maintained in a fixed position the engine will maintain its revolutions. Now if we want to move in pitch or roll, these have variable pitch propellers [35] or variable angle

of attack, which can be seen in the figure 1.8b this mechanism is common in helicopters and aircraft. To change the atack's angles only requires a servomotor that the degrees to which the propeller will be. Then how the air will be distributed for propulsion will be different. So something that has been working on these vehicles is the development of control algorithms to vary the angle of attack and achieve the stability and movement that you have with a conventional quadrotor.

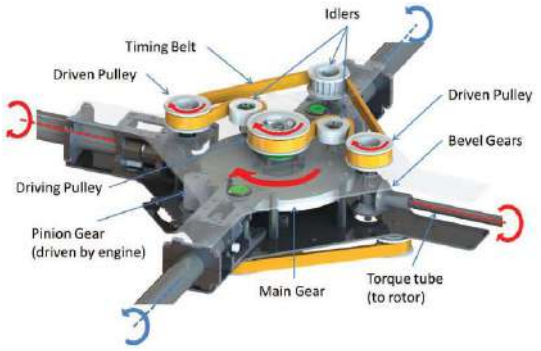

(a) Pulley mechanism to distribute power from the combustion engine to the four propellers [33].

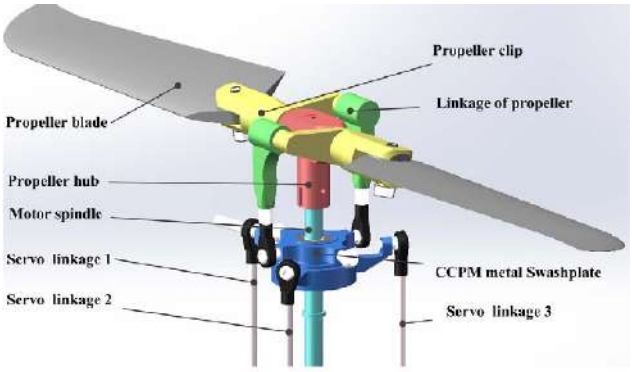

(b) Variable pitch propeller configuration, this mechanism allows moving on pitch and roll [35].

Figure 1.8: The belt-pulley mechanism that distributes the mechanical power from the combustion engine to the 4 propellers. Also the variable pitch propeller mechanism because the speed of each engine cannot be controlled to move in x, and the angle of attack must be modified, through a servomotor in each propeller.

Due to this problem, another alternative is to design mini generators that porduces the power to propel the vehicle. This mechanism consists of a combustion engine with the necessary power required by a quadrotor, then the next stage is to transform that mechanical energy into electrical energy. For a very low KV brushless motor requires few revolutions to generate electricity but high torque. The next stage is the rectification, because the motors are three-phase, the rectification stage is very important in this system, with the following objectives:

1. Converting a three-phase system to a dc system.
2. Current or voltage regulation.
3. Correct the power factor and maintain it at a value close to one.

4. Eliminate the presence of harmonics in the current.

The system have two controls: The first is a speed control due to atmospheric pressure variations in the engine. The second control is for the rectification stage because a conventional rectifier cannot be used due to the generation of harmonics at the input of the system, which causes a low power factor and damage to the source due to heating. The Figure (1.9) shows two generators used in multirotors and currently available on the market.

(a) Walkera's first mini-generator prototype may be capable of being used in demanding quadrotors, mainly in surveillance and agricultural tasks [36].

(b) Second version of walkera minigenerator [36].

Figure 1.9: The first and second model of electric generator was marketed by the company Walkera, which is the leading company in creating these electric generators.

Subsystems of an electric mini-generator for quadrotors

Based on the work of [37] and [38] who has designed a minigerator for quadrotors, they propose to divide the system as follows in three susbsections.

The first subsystem is composed of a combustion engine, either four-stroke or two-stroke, which is in charge of mechanical power generation. The first is less complex engines because they have fewer components, they are engines with high revolutions, lower torque and operate from fuel with oil mixture. They work with glow plugs because the explosion temperature is lower than that of gasoline which requires no control for the crankshaft position. As a disadvantage, they are engines that are usually more polluting and simple

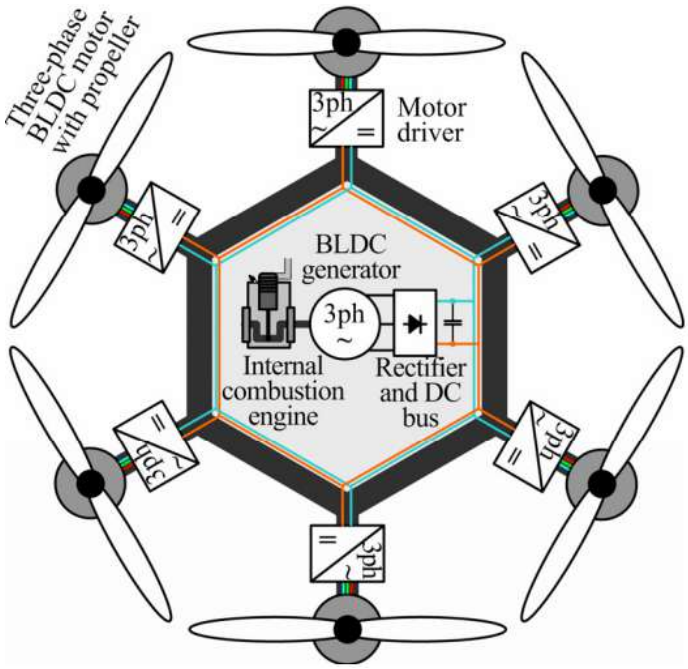

Figure 1.10: Diagram of the integration of a mini-generator from a brushless motor, for use in multirotors [37].

in the control algorithms that can be applied. For the implementation in generators it is necessary to implement gears-transmission to reduce the speed and increase the torque. On the contrary with 4-stroke engines, although they are engines with more components, they are engines with low revolutions, high torque and they run on gasoline which reduces the fuel cost.

The second stage is the conversion of mechanical energy into electrical energy by coupling a brushless motor. These motors are used in UAVs and operate with alternating current (AC). Now, since the brushless motor is not the one that generates the movement, but rather it receives the revolutions of the combustion engine, this now works as an electric generator and now the output of this motor is a three-phase AC signal. The brushless motors are classified by their KV (revolutions per voltage) refers to the constant of revolutions of a motor, in short, the number of revolutions per minute (rpm) that will be able to offer when applied 1V (one volt) voltage. This number depends on many factors such as the number of turns, diameter of the copper wire used in the winding, power of the magnets and geometry of the motor. A high KV motor offers a higher number of revolutions and these are used in racing quadrotors, they are motors with higher torque by which are used

in larger quadrotors or that require loading some external mass. When using a brushless motor as a generator, a low KV motor should be used, because it requires less rpm to start producing voltage, and because it has more torque it will be able to supply the necessary amperage for the quadrotor.

Finally, the third subsystem consists of the rectification stage of the system. A quadrotor works from a dc voltage, for this reason it is necessary to rectify the signal obtained from the brushless motors in addition to regulating the voltage or current. There are two main types of rectifiers, controlled and uncontrolled both serve to convert ac signals to dc. The difference lies in the efficiency and cost of the circuit, the controlled rectifiers are usually more expensive than the uncontrolled because, in addition to integrating the diodes, it must also integrate transistors to control the pulse that will reduce noise in the signals and regulate the voltage. An uncontrolled rectifier is usually much more economical but this produces harmonics at the input of the rectifier, which causes power losses and heating in the lines by which it is necessary to add filters. The uncontrolled rectifier by itself can not regulate the voltage or current for which requires a buck-boost circuit, this is an active circuit that requires a pwm signal to regulate the voltage, to require a pwm signal is necessary to implement a control algorithm that takes as reading the output voltage of the system. In the work of [37] an uncontrolled rectifier is used in figure (1.11) in which there is the problem of voltage regulation, without the ability to take into account the variable load of the UAV. Later in the work [38], a buck-boost circuit showed inf figure (1.12). is implemented to regulate the voltage and current in the rectifier, however, it is necessary to add a filter to avoid power factor problems.

1.2 Problem definition

The flight autonomy of UAVs is one of the main problems limiting the tasks they can perform. Having flights of 15 - 20 minutes plus the time it takes to charge a battery. In the previous section, we studied some of the strategies that have been taken to optimize flight time, alternative sources of power generation, concluding with the implementation of three phase brushless generators.

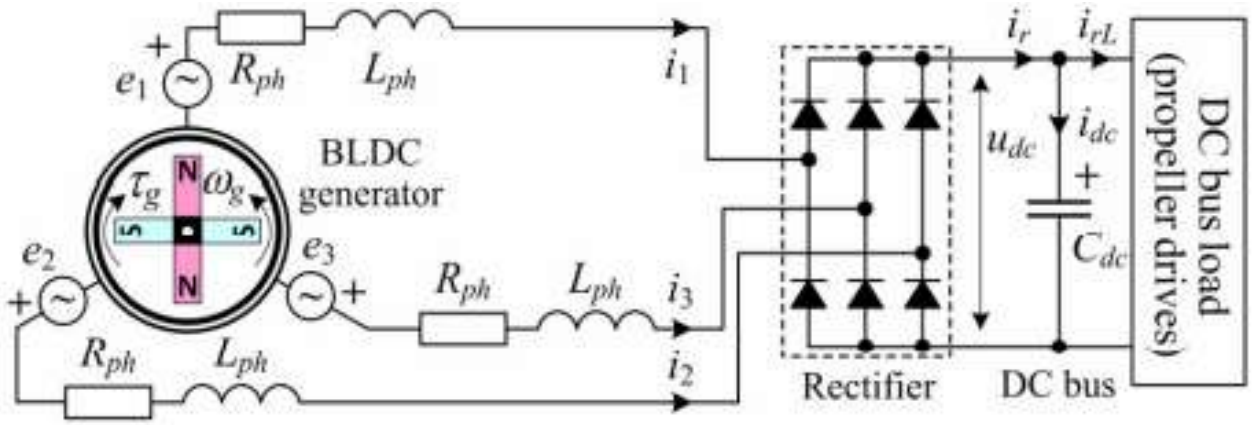

Figure 1.11: The electrical and electronic system of the mini-generator, the electrical part is integrated by the brushless motor that delivers three phases of voltage in alternating current, because of this it must go through a rectification stage. The electronic part is integrated by an uncontrolled rectifier, this does not allow to regulate of the voltage and requires external filters at the input of the rectifier to avoid distortions in the current and the appearance of harmonics [37].

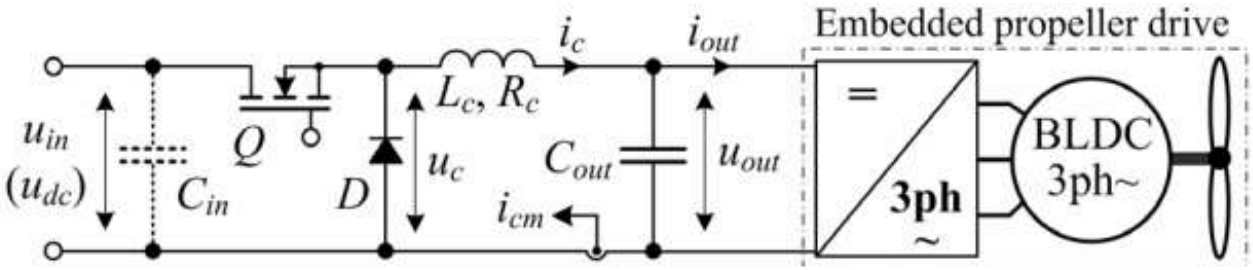

Figure 1.12: Buck-boost circuit used to regulate the DC voltage obtained from the rectifier, despite regulating the voltage it is not able to correct the harmonics at the rectifier input [38].

1.2.1 Problem statement

Brushless generators produce three-phase currents that must be rectified and regulated for use in quadcopters. The main problem with uncontrolled rectifiers is that they do not regulate voltage or current and are harmonic generators, having power losses. The implementation of controlled three-phase rectifiers can regulate voltage or current and reduce power losses. Controlled rectifiers require a control algorithm for their operation, so they are more complex in their operation. It should also be considered that the rectifier must contemplate that the quadrotor's load value is unknown and can change its value. Because of this, we propose the implementation of a robust adaptive control that considers disturbances in the output of the system as well as possible changes in the load.

1.3 Justification and objectives of the thesis

1.3.1 Justification

quadrotors applications have increased in recent years with flight time being one of the main constraints on task performance. For this reason, a modular device is required to increase flight time autonomy.

1.3.2 Main objective

The main objective of this project is to model a controlled three-phase rectifier as well as to design a robust adaptive control for voltage regulation. It also establishes the basis for the construction of a prototype of a three-phase generator for quadrotor applications.

1.3.3 Specific Objectives

- Mathematical modeling of a controlled three-phase rectifier
- Design a robust adaptive controller for voltage regulation and output load estimation.
- Perform tests of the proposed control
- Perform a software in the loop simulation for adaptive robust control
- Design and build a prototype generator for quadrotor applications.

1.4 Hypothesis

The implementation of a robust adaptive control in a controlled rectifier will allow the regulation of the voltage or current as desired, even when the output load is unknown and variable.

CHAPTER 2

Theoretical background

The analysis of the rectifier regulator is a very studied subject in both single-phase and three-phase applications due to its multiple utilities [39–41]. Some of the problems in three-phase rectifiers are the appearance of harmonics in the current and the correction of the power factor [42, 43], this is because the uncontrolled rectifiers are harmonic generators, resulting in power losses. Of equal interest is the regulation of the output voltage or current to avoid damage caused by non-regulation in the range of the equipment that uses it. Currently regulating the current and voltage, in addition to maintaining power factors close to one, is an open problem, now adding external problems such as disturbances and unknown variable loads. In this work, an adaptive robust control is proposed for a controlled three-phase rectifier of six switches which solves the problem of voltage and current regulation, in addition to maintaining the reactive current at zero, which allows maintaining power factors close to one.

There are two main classes of rectifiers: uncontrolled rectifiers [44] and controlled rectifiers [45]. The first class has the disadvantage of generating harmonics on the AC bus, which results in power losses and even damage to the equipment. Among the advantages of controlled rectifiers are power factor correction, voltage and current regulation. Due to

the nature of the system this is nonlinear, therefore in the literature several nonlinear strategies have been proposed to achieve system stability, differing the states to be controlled. The following are works related to the control of three-phase rectifiers whose objectives are different. Nonlinear controllers have been proposed for current regulation [46] and to a lesser extent for voltage regulation since it becomes more complex the voltage distribution in its control. Within the literature, sliding mode control has been proposed [47–51], its application stands out when there is a variation or unbalances in some parameters such as the output load or capacitor, it takes into account possible bad measurements in some states. The sliding mode technique allows voltage regulation in situations that cause undershoot or overshoot disturbances in the voltage output. Another method used, although to a lesser extent, is the back steeping control [52], which focuses on reducing the harmonic distortion caused by loads disturbances or the nature of the system itself. The passivity-based control [53, 54] has the advantage of using few parameters has good dynamic characteristics and high accuracy of current control, and great robustness to high and low frequencies. Now due to demand in automotive, renewable energy, and aerospace systems, predictive controllers are employed to smoothly regulate the DC voltage in the presence of fast frequencies, works on electrical generators that has used from the mechanical energy produced by the turbine of an aircraft, this energy is then used to power the aircraft electronics. Lyapunov stability analysis has been extended for predictive controllers to determine the optimal voltage vector [55]. Although some nonlinear controllers have been designed with a tested stability limit [56, 57], but the given limit for the grid current below a specific value is still not guaranteed. Finally, and the control technique of interest is adaptive controls. Adaptive control is used when the system parameters are unknown [58–60], this parameter can be some impedance, capacitance, usually considered when the output load is unknown, for example, the work of [61] is proposed to regulate the output voltage of the dc-link as well as follow a desired current reference for three-phase power rectifiers. More specifically, an efficient adaptive controller is established in the outer loop to regulate the output voltage of the dc-link in the presence of external disturbances. For control design and modeling several papers report the use of the synchronous d-q transform to model the circuit, in addition, it is common to use the d-q model for control design [62].

Table 2.1: Comparison of related state-of-the-art research.

Feature	[NLAC]	[58]	[46]	[60]
Voltage regulation	✓	✓	✗	✓
Current regulation	✓	✗	✓	✓
Control technique	Adaptive nonlinear control	Output-feedback nonlinear adaptive	Nonlinear	Adaptive
Lyapunov analisys	✓	✓	✓	✓
d-q transform	✓	✓	✓	✓
SITL	✓	✓	✓	✗
real test	✗	✗	✗	✗
Stability	Globally exponentially	Globally exponentially	None	Locally asymptotically

As mentioned above, in this work, adaptive nonlinear control is implemented using the d-q form to regulate the output voltage and control the output current.

Table 2.1 shows a comparison between the characteristics of some of the most relevant state-of-the-art controls and the one proposed in this work.

CHAPTER 3

Methodology

3.1 Modeling

In this section, we develop the mathematical model used for control purposes from the voltage equation of Fig. 3.1.

Let consider that the input AC voltage is a balanced three-phase supply given by

$$\begin{aligned} e_a(t) &= E_m \cos(\omega t) \\ e_b(t) &= E_m \cos\left(\omega t - \frac{2\pi}{3}\right) \\ e_c(t) &= E_m \cos\left(\omega t + \frac{2\pi}{3}\right), \end{aligned} \tag{3.1}$$

where E_m is the phase voltage's amplitude and ω is the angular frequency; both correspond to the power source. From Figure (3.1) it is easily to get the following time-dependent

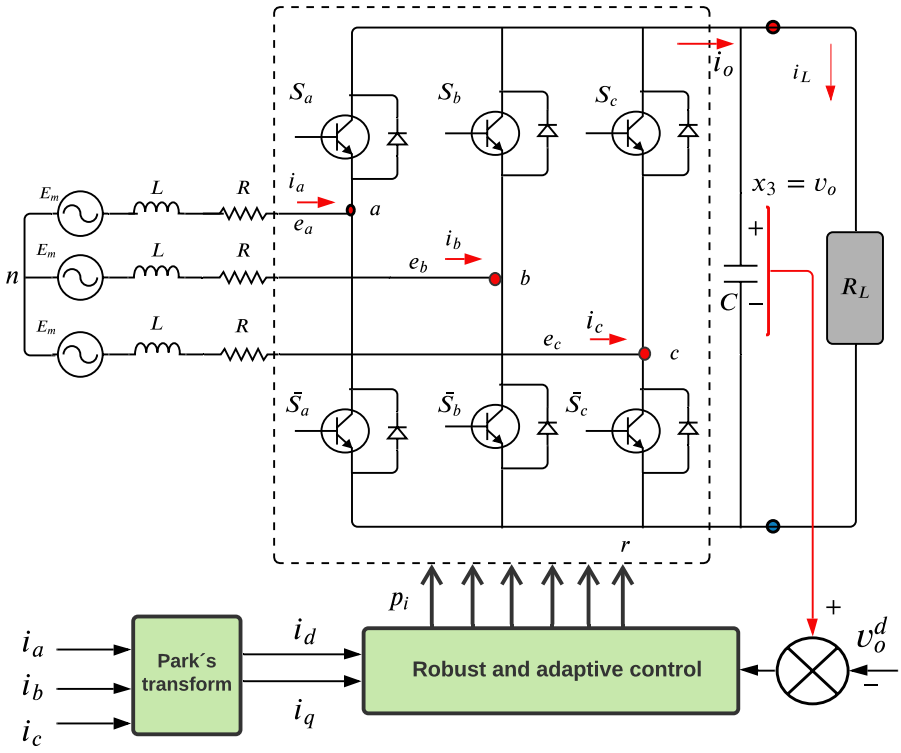

Figure 3.1: Three-phase rectifier model. For several critical applications, the electrical load represented by R_L slowly varies in time. To cope with it, we propose an adaptive control approach.

differential equations

$$\Sigma : \begin{cases} L\frac{d}{dt}i_a = -Ri_a - \frac{1}{2}p_a v_o + e_a(t) \\ L\frac{d}{dt}i_b = -Ri_b - \frac{1}{2}p_b v_o + e_b(t) \\ L\frac{d}{dt}i_c = -Ri_c - \frac{1}{2}p_c v_o + e_c(t) \end{cases} \tag{3.2}$$

$$\Omega : \left\{ C\frac{d}{dt}v_o = \frac{1}{2}\left(p_a i_a + p_b i_b + p_c i_c\right) - \frac{1}{R_L}v_o, \right. \tag{3.3}$$

where subsystem Σ represents the three-phase current, and subsystem Ω is the dynamics of the DC output voltage. The resistance and inductance of the boosting inductor are given by R and L, respectively. C is the capacity of the DC side filter capacitor; R_L is the resistive load. The input line currents are i_a, i_b, i_c, while the output DC voltage is v_o. The p_a, p_b, p_c

are bipolar functions defined as

$$p_i = \begin{cases} +1, \ S_i \text{ closed}, \\ -1, \ \bar{S}_i \text{ closed}, \end{cases} \quad \text{for } i = \{a, b, c\} \tag{3.4}$$

where S_i and $\bar{S}_i$ represent the switching function conducted by the semiconductor switch in the rectifier.

Since equations(3.2)-(3.3) are time-varying differential equations, they result to be not amenable to analysis and control design. Thus, it is desirable to transform equations (3.2)-(3.3) to time-invariant differential equations. With this aim, we use a linear transformation called the *Park's transformation* [63], [64]. The Park's transformation converts the $a - b - c$ variables to the so-called $d - q - 0$ variables. Such a transformation is given by

$$P = \frac{2}{3} \begin{pmatrix} \cos(\omega t) & \cos\left(\omega t - \frac{2\pi}{3}\right) & \cos\left(\omega t + \frac{2\pi}{3}\right) \\ \sin(\omega t) & \sin\left(\omega t - \frac{2\pi}{3}\right) & \sin\left(\omega t + \frac{2\pi}{3}\right) \\ 1/2 & 1/2 & 1/2 \end{pmatrix} \tag{3.5}$$

with inverse given by

$$P^{-1} = \begin{pmatrix} \cos(\omega t) & \sin(\omega t) & 1 \\ \cos\left(\omega t - \frac{2\pi}{3}\right) & \sin\left(\omega t - \frac{2\pi}{3}\right) & 1 \\ \cos\left(\omega t + \frac{2\pi}{3}\right) & \sin\left(\omega t + \frac{2\pi}{3}\right) & 1 \end{pmatrix}. \tag{3.6}$$

For the following computation we will use $\frac{d}{dt}P^{-1}$ given by

$$\frac{d}{dt}P^{-1} = \begin{pmatrix} -\omega \sin(\omega t) & \omega \cos(\omega t) & 0 \\ -\omega \sin\left(\omega t - \frac{2\pi}{3}\right) & \omega \cos\left(\omega t - \frac{2\pi}{3}\right) & 0 \\ -\omega \sin\left(\omega t + \frac{2\pi}{3}\right) & \omega \cos\left(\omega t + \frac{2\pi}{3}\right) & 0 \end{pmatrix}. \tag{3.7}$$

To transform the system (Σ, Ω) to a time-invariant differential equations, we proceed as follows. Let us begin with subsystem (Σ) in (3.2). The transformation from $a - b - c$

variables to $d-q-0$ variables through the Park's transform is as follows:

$$\begin{pmatrix} i_d \\ i_q \\ 0 \end{pmatrix} = P \underbrace{\begin{pmatrix} i_a \\ i_b \\ i_c \end{pmatrix}}_{i_s}, \quad \begin{pmatrix} p_d \\ p_q \\ 0 \end{pmatrix} = P \underbrace{\begin{pmatrix} p_a \\ p_b \\ p_c \end{pmatrix}}_{p_s}. \tag{3.8}$$

Notice that subsystem Σ can be represented in vector form as follows:

$$L\frac{d}{dt}\begin{pmatrix} i_a & 0 & 0 \\ 0 & i_b & 0 \\ 0 & 0 & i_c \end{pmatrix} = -\begin{pmatrix} R & 0 & 0 \\ 0 & R & 0 \\ 0 & 0 & R \end{pmatrix}\begin{pmatrix} i_a \\ i_b \\ i_c \end{pmatrix} - \frac{1}{2}\begin{pmatrix} p_a \\ p_b \\ p_c \end{pmatrix} v_o + \begin{pmatrix} e_a(t) \\ e_b(t) \\ e_c(t) \end{pmatrix}.$$

By using the Park's transformation (3.5) and equation (3.8), from the last equation we compute the following:

$$\begin{aligned} LP\frac{d}{dt}\left[\left(P^{-1}P\right)\begin{pmatrix} i_a \\ i_b \\ i_c \end{pmatrix}\right] = -P\begin{pmatrix} R & 0 & 0 \\ 0 & R & 0 \\ 0 & 0 & R \end{pmatrix} P^{-1}P\begin{pmatrix} i_a \\ i_b \\ i_c \end{pmatrix} \\ - \frac{1}{2}P\begin{pmatrix} p_a \\ p_b \\ p_c \end{pmatrix} v_o + P\begin{pmatrix} e_a(t) \\ e_b(t) \\ e_c(t) \end{pmatrix} \end{aligned} \tag{3.9}$$

and then,

$$\begin{aligned} LP\frac{d}{dt}\left[P^{-1}\begin{pmatrix} i_d \\ i_q \\ 0 \end{pmatrix}\right] = -\begin{pmatrix} R & 0 & 0 \\ 0 & R & 0 \\ 0 & 0 & R \end{pmatrix}\begin{pmatrix} i_d \\ i_q \\ 0 \end{pmatrix} \\ - \frac{1}{2}\begin{pmatrix} p_d \\ p_q \\ 0 \end{pmatrix} v_o + \begin{pmatrix} E_m \\ 0 \\ 0 \end{pmatrix}, \end{aligned} \tag{3.10}$$

since $aPI_{3\times3}P^{-1} = aI_{3\times3}$ for any $a \in \mathbb{R}$ where $I_{3\times3}$ is the identity matrix of dimension three;

and $P\begin{pmatrix} e_a(t) \\ e_b(t) \\ e_c(t) \end{pmatrix} = \begin{pmatrix} E_m \\ 0 \\ 0 \end{pmatrix}$ holds from (3.1) and (3.5). Finally, from the last expression one gets

$$\begin{aligned} L\begin{pmatrix} \frac{di_d}{dt} \\ \frac{di_q}{dt} \\ \frac{d0}{dt} \end{pmatrix} = &-\begin{pmatrix} R & 0 & 0 \\ 0 & R & 0 \\ 0 & 0 & R \end{pmatrix}\begin{pmatrix} i_d \\ i_q \\ 0 \end{pmatrix} - \frac{1}{2}\begin{pmatrix} p_d \\ p_q \\ 0 \end{pmatrix} v_o \\ &+ \begin{pmatrix} E_m \\ 0 \\ 0 \end{pmatrix} - \begin{pmatrix} \omega L i_q \\ -\omega L i_d \\ 0 \end{pmatrix} \end{aligned} \tag{3.11}$$

since $LP\frac{d}{dt}P^{-1}\begin{pmatrix} i_d \\ i_q \\ 0 \end{pmatrix} = \begin{pmatrix} \omega L i_q \\ -\omega L i_d \\ 0 \end{pmatrix}$ holds from (3.7). Therefore, the system of equations are:

$$\Sigma^{i_d,i_q}: \begin{cases} \frac{di_d}{dt} = -\frac{R}{L}i_d - \frac{1}{2L}p_d v_o - \omega i_q + \frac{E_m}{L} \\ \frac{di_q}{dt} = -\frac{R}{L}i_q - \frac{1}{2L}p_q v_o + \omega i_d. \end{cases} \tag{3.12}$$

On the other hand, notice that the measured voltages from the ground to the nodes a, b, c in the circuit diagram depicted in Fig. 3.1 are given as [65]

$$v_{ag} = \frac{1}{2}(1+p_a)v_o,\ v_{bg} = \frac{1}{2}(1+p_b)v_o,\ v_{cg} = \frac{1}{2}(1+p_c)v_o. \tag{3.13}$$

From a simple circuit analysis, it is noted that $i_a + i_b + i_c = 0$ (see Fig. 3.1). Therefore, the output current can be computed as [65]

$$i_o = \frac{1}{2}p_s^{\intercal} i_s. \tag{3.14}$$

Thus, from (3.8) we can express i_o in (3.14) in the $d-q-0$ frame as follows

$$i_o = \frac{1}{2}\left(P^{-1}\begin{pmatrix} p_d \\ p_q \\ 0 \end{pmatrix}\right)^{\intercal} P^{-1}\begin{pmatrix} i_d \\ i_q \\ 0 \end{pmatrix} = \frac{3}{4}\left(p_d i_d + p_q i_q\right). \tag{3.15}$$

Then, from the Kirchhoff's current law (1st Law) one gets

$$i_o = i_L + C\frac{dv_o}{dt}. \tag{3.16}$$

Finally, combining (3.15) with (3.16) and using the Ohm's law the dynamics of the output DC voltage is

$$\Omega^{i_d,i_q} : \begin{cases} \frac{d}{dt}v_o = \frac{3}{4C}\left(p_d i_d + p_q i_q\right) - \frac{1}{R_L C}v_o. \end{cases} \tag{3.17}$$

Therefore, the complete system is

$$\Sigma^{i_d,i_q} : \begin{cases} \frac{di_d}{dt} = -\frac{R}{L}i_d - \frac{1}{2L}p_d v_o - \omega i_q + \frac{E_m}{L} \\ \frac{di_q}{dt} = -\frac{R}{L}i_q - \frac{1}{2L}p_q v_o + \omega i_d \end{cases} \tag{3.18}$$

$$\Omega^{i_d,i_q} : \begin{cases} \frac{dv_o}{dt} = \frac{3}{4C}\left(p_d i_d + p_q i_q\right) - \frac{1}{R_L C}v_o. \end{cases} \tag{3.19}$$

Now, let consider the case where the output DC voltage is disturbed by exogenous signals varying with time. This scenario is given when noise or voltage variations due to changes in the load are presented. We model the unknown voltage variations as an unknown disturbance $\delta(t)$. Thus, the output model voltage is given by:

$$\Omega^{i_d,i_q,\delta} : \begin{cases} \frac{d}{dt}v_o = \frac{3}{4C}\left(p_d i_d + p_q i_q\right) - \frac{1}{R_L C}v_o + \delta(t). \end{cases} \tag{3.20}$$

3.2 Control

The system under study and developed in the previous section is summarized next

$$\Sigma^{i_d,i_q}: \begin{cases} \frac{di_d}{dt} = -\frac{R}{L}i_d - \frac{1}{2L}p_d v_o - \omega i_q + \frac{E_m}{L} \\ \frac{di_q}{dt} = -\frac{R}{L}i_q - \frac{1}{2L}p_q v_o + \omega i_d \end{cases} \tag{3.21}$$

$$\Omega^{i_d,i_q,\delta}: \begin{cases} \frac{dv_o}{dt} = \frac{3}{4C}\left(p_d i_d + p_q i_q\right) - \frac{1}{R_L C}v_o + \delta(t). \end{cases} \tag{3.22}$$

By considering the system $(\Sigma^{i_d,i_q}, \Omega^{i_d,i_q,\delta})$ we tackle two main problems:

Problem 1 (Robust stabilization) *Let us consider the system $(\Sigma^{i_d,i_q}, \Omega^{i_d,i_q,\delta})$, where the load resistance R_L is known. The problem is to find controllers (p_d, p_q) such that i_d converges to i_d^d, i_q converges to 0, and v_o converges to v_o^d, where (i_d^d, v_o^d) are desired values. The convergence must follow despite the presence of the unknown time-varying disturbance $\delta(t)$.*

Remark 1 *To obtain a unity power factor, the desired value for the state i_q must be zero, since e_q is zero in steady state. Therefore, i_d results to be the magnitude of the input line current.*

The problem 1 inherently considers that the parameters (R, L, C, E_m) are known. This assumption is usually easily achievable, since the manufacturer gives such values in any three-phase rectifier. The R_L is also known in a variety of applications and is given by the designer. However, in certain cases, R_L is unknown or can vary in time. This case is considered in the next problem.

Problem 2 (Robust and adaptive stabilization) *Solve the problem 1 but considering the lack of knowledge of the load R_L.*

Remark 2 *In the problems 1 and 2, due to the underactuated and bilinear nature of the system $(\Sigma^{i_d,i_q}, \Omega^{i_d,i_q,\delta})$, it is only possible to stabilize i_d or v_o to an arbitrary desired value, not both at the same time. Thus, one can design controllers to stabilize the output DC*

voltage v_o, or the d-axis line current i_d. In any case, the designer proposes i_d^d (v_o^d), while v_o^d (i_d^d) is computed following the system restrictions;

Let us consider the following error definition:

$$e_1 = i_d - i_d^d,\ e_2 = i_q,\ e_3 = v_o - v_o^d \tag{3.23}$$

with dynamics given by,

$$\begin{aligned}
\dot{e}_1 &= -\frac{R}{L}\left(e_1 + i_d^d\right) - \omega e_2 - \underbrace{\frac{1}{2L}\left(e_3 + v_o^d\right) p_d}_{u_1} + \frac{E_m}{L} \\
\dot{e}_2 &= -\frac{R}{L} e_2 + \omega\left(e_1 + i_d^d\right) - \frac{1}{2L}\left(e_3 + v_o^d\right) p_q \\
\dot{e}_3 &= \underbrace{\frac{3}{4C}\left(e_1 + i_d^d\right) p_d}_{u_2} + \frac{3}{4C} e_2 p_q - \frac{1}{R_L C}\left(e_3 + v_o^d\right) + \delta(t).
\end{aligned} \tag{3.24}$$

It is assumed that the unknown exogenous disturbance $\delta(t)$ in (3.24) meets the following.

Assumption 1 *The unknown time-varying disturbance in* (3.24) *is bounded as,*

$$|\delta(t)| \leq c\sqrt{|e_3|}, \tag{3.25}$$

where c is a positive constant.

The first main result is summarized in the following proposition.

Proposition 1 (Robust controller) *Let us consider the perturbed error system given by* (3.24) *with virtual control inputs defined by:*

$$\frac{1}{2L}\left(e_3 + v_o^d\right) p_d := u_1,\ \ \frac{3}{4C}\left(e_1 + i_d^d\right) p_d := u_2, \tag{3.26}$$

with desired values (v_o^d, i_d^d) chosen as it is explained in remark 3 and that the assumption

1 holds. Then, the control law

$$\begin{aligned} u_1 &= -\frac{R}{L}\left(e_1 + i_d^d\right) - \omega e_2 + \frac{E_m}{L} + k_1\sqrt{|e_1|}\,\mathrm{sgn}\,(e_1) \\ u_2 &= -\frac{3}{4C}e_2 p_q + \frac{1}{R_L C}\left(e_3 + v_o^d\right) - k_3\sqrt{|e_3|}\,\mathrm{sgn}\,(e_3) \end{aligned} \tag{3.27}$$

where,

$$p_q = \frac{2L}{e_3 + v_o^d}\Big(-\frac{R}{L}e_2 + \omega(e_1 + i_d^d) + k_2\sqrt{|e_2|}\,\mathrm{sgn}\,(e_2)\Big) \tag{3.28}$$

and $k_1 > 0$, $k_2 > 0$, *and* $k_3 > c$, *globally stabilizes the origin* $[e_1, e_2, e_3]^\intercal = [0, 0, 0]^\intercal$ *in finite time.*

proof 1 *Let consider the candidate Lyapunov function,* $V = |e_1| + |e_2| + |e_3|$ *with time-derivative along the trajectories of the error system* (3.24) *computed as:*

$$\begin{aligned} \dot{V} &= \mathrm{sgn}\,(e_1)\dot{e}_1 + \mathrm{sgn}\,(e_2)\dot{e}_2 + \mathrm{sgn}\,(e_3)\dot{e}_3 \\ &= \mathrm{sgn}\,(e_1)\Big(-\frac{R}{L}\left(e_1 + i_d^d\right) - \omega e_2 - u_1 + \frac{E_m}{L}\Big) \\ &\quad + \mathrm{sgn}\,(e_2)\Big(-\frac{R}{L}e_2 + \omega\left(e_1 + i_d^d\right) - \frac{1}{2L}\left(e_3 + v_o^d\right)p_q\Big) \\ &\quad + \mathrm{sgn}\,(e_3)\Big(u_2 + \frac{3}{4C}e_2 p_q - \frac{1}{R_L C}\left(e_3 + v_o^d\right) + \delta(t)\Big). \end{aligned} \tag{3.29}$$

We substitute the control law (3.27) *in the previous expression, and it follows that*

$$\begin{aligned} \dot{V} &= \mathrm{sgn}\,(e_1)\Big(-k_1\sqrt{|e_1|}\,\mathrm{sgn}(e_1)\Big) \\ &\quad + \mathrm{sgn}\,(e_2)\Big(-k_2\sqrt{|e_2|}\,\mathrm{sgn}\,(e_2)\Big) \\ &\quad + \mathrm{sgn}\,(e_3)\Big(-k_3\sqrt{|e_3|}\,\mathrm{sgn}\,(e_3) + \delta(t)\Big), \end{aligned} \tag{3.30}$$

and from assumption 1 it follows that

$$\dot{V} \leq -k_1\sqrt{|e_1|} - k_2\sqrt{|e_2|} - (k_3 - c)\sqrt{|e_3|}. \tag{3.31}$$

Besides, it's known that $-\sum_{i=1}^n |x_i|^{1/2} \leq -\sqrt{\sum_{i=1}^n |x_i|}$ *hence* $\dot{V} \leq -\min\{k_1, k_2, k_3\}\sqrt{|e_1| + |e_2| + |e_3|}$. *If we choose* $a = \min\{k_1, k_2, k_3\}$, *then,* $\dot{V} \leq -a\sqrt{V}$ *and the origin* $[e_1, e_2, e_3]^\intercal = [0, 0, 0]^\intercal$ *is*

globally stable with convergence in finite time.

Remark 3 *Notice that virtual controls* (u_1, u_2) *in* (3.26) *are both functions of the real control input* p_d*. This fact implies two important things: a) it is only possible to control the DC voltage* v_o*, or the* d*-axis line current, as it was explained in remark 2; and b) when one arbitrarily chooses* v_o^d *(respectively,* i_d^d*) the desired value of* i_d^d*, (respectively,* v_o^d*) must be*

$$i_d^d = \frac{4(v_o^d)^2}{6LR_L\alpha},\ \left(v_o^d = \pm\sqrt{\frac{6LR_L\alpha i_d^d}{4}}\right) \tag{3.32}$$

with $\alpha = -\frac{R}{L}i_d^d + \frac{E_m}{L}$*. The latter desired values can be easily computed from* (3.26) *and* (3.27) *when the closed-loop system has converged, i.e., for* $t \geq t^*$*, where* t^* *is the convergence time.*

3.2.1 Robust and adaptive control

Despite the robust controller (3.27) achieves to stabilize the error system (3.24) under external disturbance $\delta(t)$, it is sometimes required to control AC/DC converters where the resistive load (R_L) is unknown or even can slowly vary with time. In such scenarios, the controller (3.27) cannot present satisfactory results. With that aim, in this section, we propose an adaptive and robust control that can cope with situations in which the resistive load is unknown, and the external disturbances alter the output voltage. Thus, the following analysis provide a solution to the problem 2.

Proposition 2 (Adaptive and robust control) *Consider the errors for system* $(\Sigma^{i_d,i_q}, \Omega^{i_d,i_q,\delta})$ *defined by*

$$\tilde{e}_1 = i_d - i_d^d,\ \tilde{e}_2 = i_q,\ \tilde{e}_3 = v_o - v_o^m, \tag{3.33}$$

with dynamics

$$\begin{aligned}
\dot{\tilde{e}}_1 &= -\frac{R}{L}\left(\tilde{e}_1 + i_d^d\right) - \omega\tilde{e}_2 - \underbrace{\frac{1}{2L}\left(\tilde{e}_3 + v_o^m\right)p_d}_{u_1} + \frac{E_m}{L} \\
\dot{\tilde{e}}_2 &= -\frac{R}{L}\tilde{e}_2 + \omega\left(\tilde{e}_1 + i_d^d\right) - \frac{1}{2L}\left(\tilde{e}_3 + v_o^m\right)p_q \\
\dot{\tilde{e}}_3 &= \underbrace{\frac{3}{4C}\left(\tilde{e}_1 + i_d^d\right)p_d}_{u_2} + \frac{3}{4C}\tilde{e}_2 p_q - \frac{1}{R_L C}\left(\tilde{e}_3 + v_o^m\right) \\
&\qquad + \delta(t) + a_m v_o^m - b_m u^m.
\end{aligned} \tag{3.34}$$

together with the model reference for subsystem $\Omega^{i_d,i_q,\delta}$ given by

$$\dot{v}_o^m = -a_m v_o^m + b_m u^m, \tag{3.35}$$

where (a_m, b_m) are positive real numbers arbitrarily chosen with control [1]

$$u^m = \frac{1}{b_m}\Big(v_o^d + a_m v_o^m - \kappa^m\left(v_o^m - v_o^d\right)\Big) \tag{3.36}$$

where $\kappa^m > 0$. Besides, consider that the assumption 1 holds and that exists a positive constant a_m such that

$$a_m = \frac{1}{R_L C} - \Theta^* \tag{3.37}$$

with Θ^* constant. Then, the adaptive-robust control

$$\begin{aligned}
p_q &= \frac{2L}{\tilde{e}_3 + v_o^m}\Big(-\frac{R}{L}\tilde{e}_2 + \omega(\tilde{e}_1 + i_d^d) + k_2\sqrt{|\tilde{e}_2|}\,\mathrm{sgn}\left(\tilde{e}_2\right)\Big) \\
u_1 &= -\frac{R}{L}\left(\tilde{e}_1 + i_d^d\right) - \omega\tilde{e}_2 + \frac{E_m}{L} + k_1\sqrt{|\tilde{e}_1|}\,\mathrm{sgn}\left(\tilde{e}_1\right) \\
u_2 &= \Theta v_o + Q^* u^m - \frac{3}{4C}\tilde{e}_2 p_q - \tilde{k}_3\sqrt{|\tilde{e}_3|}\,\mathrm{sgn}\left(\tilde{e}_3\right) \\
\dot{\Phi} &= -\lambda\tilde{e}_3 v_o
\end{aligned} \tag{3.38}$$

[1] The control (3.36) clearly globally exponentially stabilizes the equilibrium $v_o^m - v_o^d$ of the model reference system (3.35).

where $\Phi = \Theta - \Theta^*$*,* $Q^* = b_m$*,* $\lambda > 0$*,* $k_1 > 0$*,* $k_2 > 0$*, and* $\tilde{k}_3 > c$*, makes that the origin of* (3.34) *asymptotically converge in the large.*

proof 2 (Proof of Proposition 2) *The proposition is proven through the Lyapunov theory. We propose the radially unbounded candidate Lyapunov function:*

$$W = |\tilde{e}_1| + |\tilde{e}_2| + \frac{1}{2}\tilde{e}_3^2 + \frac{\lambda^{-1}}{2}\Phi^2, \tag{3.39}$$

whose time-derivative along the solutions of dynamics (3.34) *and the last equation of* (3.38) *is computed as:*

$$\begin{aligned}
\dot{W} &= \operatorname{sgn}(\tilde{e}_1)\dot{\tilde{e}}_1 + \operatorname{sgn}(\tilde{e}_2)\dot{\tilde{e}}_2 + \tilde{e}_3\dot{\tilde{e}}_3 + \lambda^{-1}\Phi\dot{\Phi} \\
&= \operatorname{sgn}(\tilde{e}_1)\Big(-\frac{R}{L}\left(\tilde{e}_1 + i_d^d\right) - \omega\tilde{e}_2 - u_1 + \frac{E_m}{L}\Big) \\
&\quad + \operatorname{sgn}(\tilde{e}_2)\Big(-\frac{R}{L}\tilde{e}_2 + \omega\left(\tilde{e}_1 + i_d^d\right) - \frac{1}{2L}\left(\tilde{e}_3 + v_o^d\right)p_q\Big) \\
&\quad + \tilde{e}_3\Big(u_2 + \frac{3}{4C}\tilde{e}_2 p_q - \frac{1}{R_L C}\left(\tilde{e}_3 + v_o^m\right) \\
&\quad + \delta(t) + a_m v_o^m - b_m u^m\Big) + \lambda^{-1}\Phi\left(-\lambda\tilde{e}_3 v_o\right).
\end{aligned} \tag{3.40}$$

Substituting the robust and adaptive control (3.38) *in the previous expression results in:*

$$\begin{aligned}
\dot{W} &= -k_1\sqrt{|\tilde{e}_1|} - k_2\sqrt{|\tilde{e}_2|} \\
&\quad + \tilde{e}_3\Big(\Theta v_o + Q^* u^m - \tilde{k}_3\sqrt{|\tilde{e}_3|}\operatorname{sgn}(\tilde{e}_3) \\
&\quad - \frac{1}{R_L C}\left(\tilde{e}_3 + v_o^m\right) + \delta(t) + a_m v_o^m - b_m u^m\Big) \\
&\quad - \lambda^{-1}\lambda\Phi\tilde{e}_3 v_o \\
&\leq -k_1\sqrt{|\tilde{e}_1|} - k_2\sqrt{|\tilde{e}_2|} - \tilde{k}_3\left(|\tilde{e}_3|\right)^{\frac{3}{2}} + |\tilde{e}_3||\delta(t)| \\
&\quad + \tilde{e}_3\Big(\Theta v_o - \frac{1}{R_L C}\left(\tilde{e}_3 + v_o^m\right) + a_m v_o^m\Big) - \lambda^{-1}\lambda\Phi\tilde{e}_3 v_o
\end{aligned} \tag{3.41}$$

and from (3.37) *and considering assumption 1 it follows that:*

$$\begin{aligned}\dot{W} &\leq -k_1\sqrt{|\tilde{e}_1|} - k_2\sqrt{|\tilde{e}_2|} - \left(\tilde{k}_3 - c\right)|\tilde{e}_3|^{\frac{3}{2}} \\ &\quad + \tilde{e}_3\Big(\Theta v_o - (a_m + \Theta^*)\, v_o + a_m v_o^m\Big) - \lambda^{-1}\lambda\Phi\tilde{e}_3 v_o \\ &\leq -k_1\sqrt{|\tilde{e}_1|} - k_2\sqrt{|\tilde{e}_2|} - \left(\tilde{k}_3 - c\right)|\tilde{e}_3|^{\frac{3}{2}} \\ &\quad + \tilde{e}_3\Big(\Phi v_o - a_m\tilde{e}_3\Big) - \Phi\tilde{e}_3 v_o \\ &\leq -k_1\sqrt{|\tilde{e}_1|} - k_2\sqrt{|\tilde{e}_2|} - \left(\tilde{k}_3 - c\right)|\tilde{e}_3|^{\frac{3}{2}} - a_m\tilde{e}_3^2 \leq 0,\end{aligned} \tag{3.42}$$

which implies that the origin in (3.34) *and the last equation of* (3.38) *is globally uniformly stable. To conclude asymptotic stability, i.e.,* $\lim_{t\to\infty}\|e(t)\| = 0$*, where* $e = [\tilde{e}_1,\ \tilde{e}_2,\ \tilde{e}_3]^\intercal$*, notice that* $-\int_{t_0}^{\infty}\dot{W}d\tau = V(t_0) - V(\infty)$ *is bounded, and therefore* $0 \leq \int_{t_0}^{\infty}\left(\sqrt{|\tilde{e}_1|} + \sqrt{|\tilde{e}_2|} + |\tilde{e}_3|^{\frac{3}{2}} + \tilde{e}_3^2\right)d\tau < \infty$*. Now, from the boundedness of* (3.34) *and the last equation of* (3.38)*, we claim the Barbalat's Lemma [66] to finally prove that* $\lim_{t\to\infty}|e(t)| = 0$*.*

Remark 4 *Notice that the convergence of* $\Theta(t)$ *to the desired value* Θ^* *depends on the persistent excitation of* u^m*. However, for the control purposes of the problem 2 it is sufficient to prove that* $\lim_{t\to\infty}\|e(t)\| = 0$*.*

3.2.2 PWM strategy

The DC link voltage v_o is controlled by control algorithms with provide the value of i_d^d, while i_q^d is fixed to zero in order to obtain power factor equal to one. These references are compared with the inputs currents wich are in dq coordinates according to equation(3.18), the controller give the values p_d and p_q. To distribute the control to the rectifier switches it is necessary to have a pwm signal, the space vector technique (svpwm) is used to perform this conversion. The complete diagram of the power generation and rectification stage is shown in the Figure (3.2), and the adaptive robust control and pwm conversion stage are better exemplified. The points of the svpwm technique are as follows:

- Determine p_α, p_β and the angle
- Determine the time duration T_n, T_{n-1} and T_z.

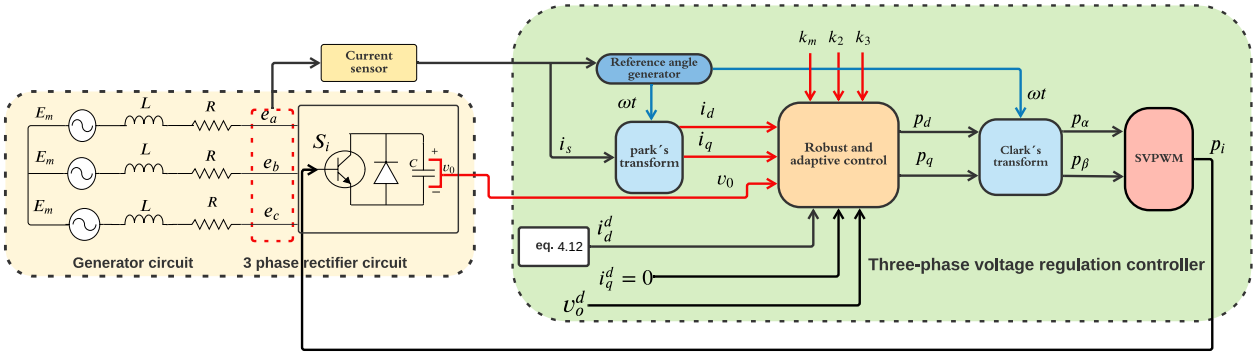

Figure 3.2: Composed of the source integrated by the voltage of each phase of the generated $[e_a, e_b, e_c]$ and the impedance given by R and L. In addition, it is also integrated by the rectifier circuit, composed of the 6 actuators p_i and a capacitor at the output to smooth the signal. The control is integrated by the Park's transformation from which we obtain i_d and i_q and by means of a sensor in v_o, we obtain v_o. The second block is the proposed controller where the error is obtained from the desired states. From this signal, we obtain two control outputs p_d and p_q, these signals must be treated to be distributed to the circuit so first the Clark's transformation is performed to apply the SVPWM technique. Finally, this pwm signal closes the loop with the circuit.

- Determine the switching time of each transistor S_1 to S_6.

The switching states of the rectifier are determined the space vector pulse-width modulation (svpwm). Given a set of three phase switch functions, the switching functions space vector is defined as:

$$p = \frac{2}{3}(p_a + up_b + u^2 p_c) \tag{3.43}$$

where $u = e^{j(\frac{2\pi}{3})}$ and is known as Park's vector. Generalizing the Park's vector the switch function are bipolar, then equation (3.43) can be writen in the generalized form for all rectifier switching states as follows:

$$p_n = \begin{cases} \frac{4}{3}e^{j(n-1)(\frac{\pi}{3})}, n = 1, 2..., 6 \\ 0, n = 7, 8 \end{cases} \tag{3.44}$$

Depending on the switching state on the circuit, the rectifier assume eight possible distinct states p_1 to p_8. p_1 to p_6 are fixed nonzero vectors, p_7 and p_8 are two zero vectors. The

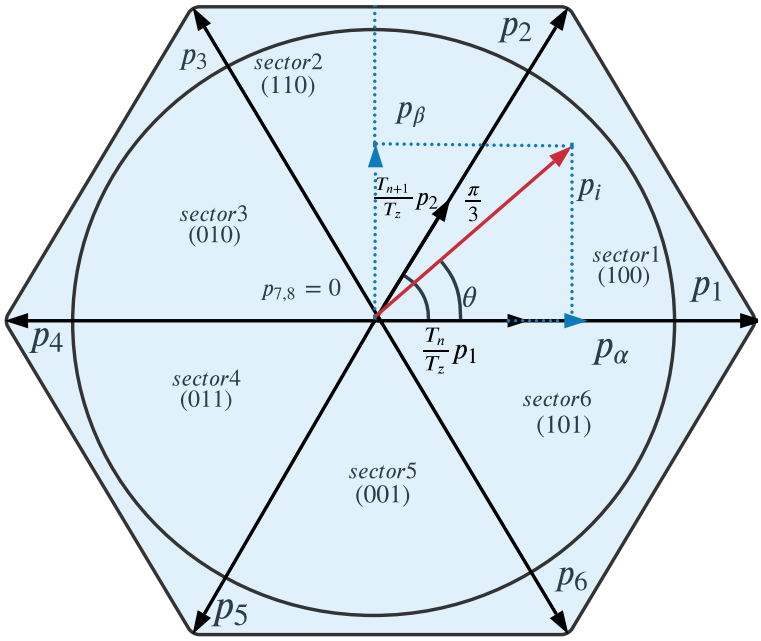

Figure 3.3: Representation of Rotating Vector in Complex Plane. This method is called hexagon because the rectifier has eight combinations of states for the activation of the switch, 6 states are nonzero p_1 to p_6 while p_7 and p_8 are zero. Then they are passed to the $\alpha\beta$ frame to obtain the pwm time in each sector.

Figure 3.3 shows the obtained states, these are the possible combinations of the rectifier switches.

Once the gate drive pulses for the switch states p_1 to p_6 have been determined, it is necessary to obtain the pulse width or pulse duration, normally in existing work one must first switch from a,b,c space to $\alpha - \beta$ space (p_a, p_b, p_c to p_α, p_β) [67] considering that one works with the model and control in a,b,c space and not in another space. In this case, the control and model were worked in the space dq for which the control outputs obtained are $p_d - p_q$ based on the work reported in [68] we switch to the space p_α p_β using Clark's transformation as follows:

$$\begin{bmatrix} p_\alpha \\ p_\beta \end{bmatrix} = \begin{bmatrix} \cos(\omega t) & -\sin(\omega t) \\ \sin(\omega t) & \cos(\omega t) \end{bmatrix} \begin{bmatrix} p_d \\ p_{q.} \end{bmatrix} \tag{3.45}$$

Where ωt = θ and can be obtained with $\theta = \tan^{-1}(\frac{p_\beta}{p_\alpha})$ and $p_i = [p_\alpha, p_\beta]^T$ and T_s is the sample time. The duration T_i, T_{i+1} and t_z of the space vector, is calculated as:

Table 3.1: The sequence of pwm activation in each transistor of the rectifier, by space vector technique.

sector	upper switches	lower switches
1	$S_a = T_n + T_{n+1} + \frac{T_z}{2}$ $S_b = T_{n+1} + \frac{T_z}{2}$ $S_c = \frac{T_z}{2}$	$\bar{S}_a = \frac{T_z}{2}$ $\bar{S}_b = T_n + \frac{T_z}{2}$ $\bar{S}_c = T_n + T_{n+1} + \frac{T_z}{2}$
2	$S_a = T_n + \frac{T_z}{2}$ $S_b = T_n + T_{n+1} + \frac{T_z}{2}$ $S_c = \frac{T_z}{2}$	$\bar{S}_a = T_{n+1} + \frac{T_z}{2}$ $\bar{S}_b = \frac{T_z}{2}$ $\bar{S}_c = T_n + T_{n+1} + \frac{T_z}{2}$
3	$S_a = \frac{T_z}{2}$ $S_b = T_n + T_{n+1} + \frac{T_z}{2}$ $S_c = T_{n+1} + \frac{T_z}{2}$	$\bar{S}_a = T_n + T_{n+1} + \frac{T_z}{2}$ $\bar{S}_b = \frac{T_z}{2}$ $\bar{S}_c = T_n + \frac{T_z}{2}$
4	$S_a = \frac{T_z}{2}$ $S_b = T_n + \frac{T_z}{2}$ $S_c = T_n + T_{n+1} + \frac{T_z}{2}$	$\bar{S}_a = T_n + T_{n+1} + \frac{T_z}{2}$ $\bar{S}_b = T_{n+1} + \frac{T_z}{2}$ $\bar{S}_c = \frac{T_z}{2}$
5	$S_a = T_{n+1} + \frac{T_z}{2}$ $S_b = \frac{T_z}{2}$ $S_c = T_n + T_{n+1} + \frac{T_z}{2}$	$\bar{S}_a = T_n + \frac{T_z}{2}$ $\bar{S}_b = T_n + T_{n+1} + \frac{T_z}{2}$ $\bar{S}_c = \frac{T_z}{2}$
6	$S_a = T_n + T_{n+1} + \frac{T_z}{2}$ $S_b = \frac{T_z}{2}$ $S_c = T_n + \frac{T_z}{2}$	$\bar{S}_a = \frac{T_z}{2}$ $\bar{S}_b = T_n + T_{n+1} + \frac{T_z}{2}$ $\bar{S}_c = T_{n+1} + \frac{T_z}{2}$

$$T_n = T_s p_i \sin\left(\frac{\pi}{3} - \theta\right) \tag{3.46}$$

$$T_{n+1} = T_s p_i \sin(\theta) \tag{3.47}$$

$$T_z = T_s - T_n - T_{n+1} \tag{3.48}$$

Let T_s denote half the switching period, that is T_s = $\frac{1}{2f_s}$, where f_s is the rectifier switching frecuency. T_n and T_{n+1} denote the ON time of the space vector for the states n and n+1. Where 0 $\leq$ p_i $\leq$ 1 is the length of the vector p_i the space vector technique selects the vector to be used and the respective sequence and time. The Table 3.1 describes the

turn-on and turn-off time of each transistor in the rectifier. The sequence establishes the symmetry of the resulting gating pulses and the distribution of the current throughout the power switches.

CHAPTER 4

Results

4.1 Experiments and simulation results

In this section, two sets of experiments are proposed to show the performance of the proposed control strategy. The first set of experiments deals with the comparison of the proposed adaptive robust control designed in this paper with another two algorithms. The first algorithm is the robust (3.27) control part (3.28) proposed in this work, while the second controller consists of a proportional-integral (PI) whose structure is mentioned in the work of [69]. In the experiments, the following elements were evaluated to measure the controller performance. Convergence speed, damping smoothness, response to external noise, response to load variation R_L. The experiments were performed considering changes in the load values R_L smoothly and without abrupt changes, in this way, it was possible to check if the control compensated for changes in the output load. A step perturbation was added at the output of the rectifier, this has different magnitudes in order to check the stability of the system with the different controllers. For the robust and adaptive control, we also added the graphs of the controller outputs as well as the i_d and i_q states. The experiments are presented in the following order: robust controller, adaptive

and robust controller (4.1), PI controller. This section of simulations was performed in MATLAB/Simulink using the power system block toolbox.

The second simulation section is a SITL corresponding to adaptive robust control. This simulation was performed using the PSpice/Simulink simulation environment show in Figure (4.10). The analog circuit was built in PSpice-capture software with the transistors corresponding to the real system model, while the digital and control part of the system is hosted in Simulink. The intention of performing this SITL is to perform preliminary tests for the implementation of a HITL and later a real implementation. In this section, the outputs of the states v_o, i_d and i_q are evaluated to their desired values, that the voltage e_s and the current i_s are in phase and without distortion and finally the generation of the pwm signal by analyzing the different stages of the controller output. For the first set of experiments, the parameters shown in Table 4.1 were used with adjustments to the gains for the PI control, while for the SITL the parameters shown in the table 4.2 were selected. In both sets of experiments, the architecture shown in Figure 3.2 was followed.

Table 4.1: Parameters used in simulink simulation for three phase rectifier control

Parameter	Value	Parameter	Value
E_m	$80V$	$k2$	2000
L	$5mH$	$k3$	4500
v_o^d	$48V$	pwm amplitude	$1V$
C	$2500\mu f$	pwm frequency	$5kHz$
ω	$60H_z$	R	0.1
a_m	15	b_m	15
k_m	2000	γ	1

4.1.1 Simulation

As mentioned in previous points, the goal of this control is to ensure that v_o manages to converge to v_o^d, regardless of whether R_L is unknown.

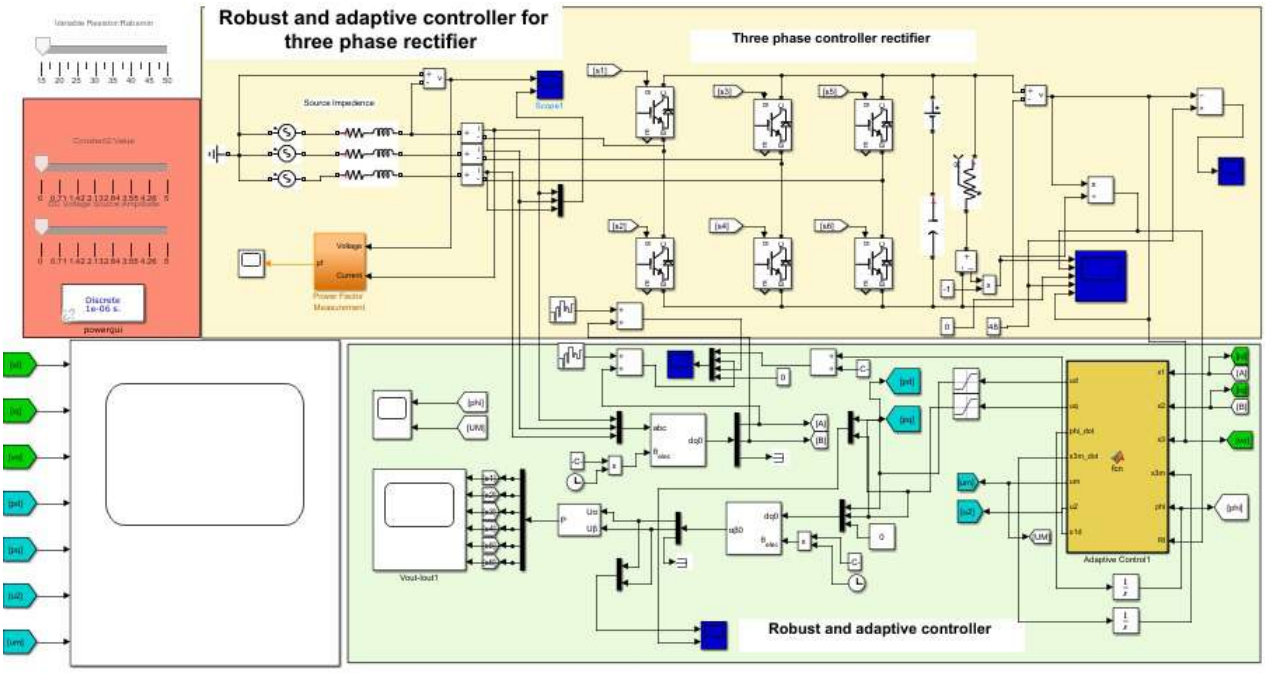

Figure 4.1: Simulation of the model with the proposed controller, yellow color shows the rectifier circuit with the electric generator. The green color shows the designed controller, integrated by the adaptive control (yellow block) and then the process to obtain the pwm signal with the space vector.

Robust controller [Proposition 1]

The first control strategy deals with the finite-time robust control proposed in this work. It should be noted that this part of the control does not contemplate an unknown R_L. For this control, the states corresponding to the equations (3.17) and (3.18) are considered. These are obtained from the fact that the currents i_s pass through the Park's transformation block represented in the equations (3.5). A simulation time of 3s is considered. The results of the experiment are shown in Figure 4.2. There are four plots, the first one represents v_o and v_o^d, the second one i_o, in these two experiments we look for the signals to converge to the desired value in case of v_o and to the calculated value in case of i_o the third one shows a step perturbation added in the output system and finally, the fourth plot shows the variation added in R_L. During this test, a convergence of less than 0.25s was obtained. In the first 0.5s, the value of R_L was kept fixed at $45\ \Omega$, and perturbations were added to the system with magnitudes from 1 to 5V. In this first part in which the load was not varied, the convergence of the control was smooth, peaks were obtained in v_o and

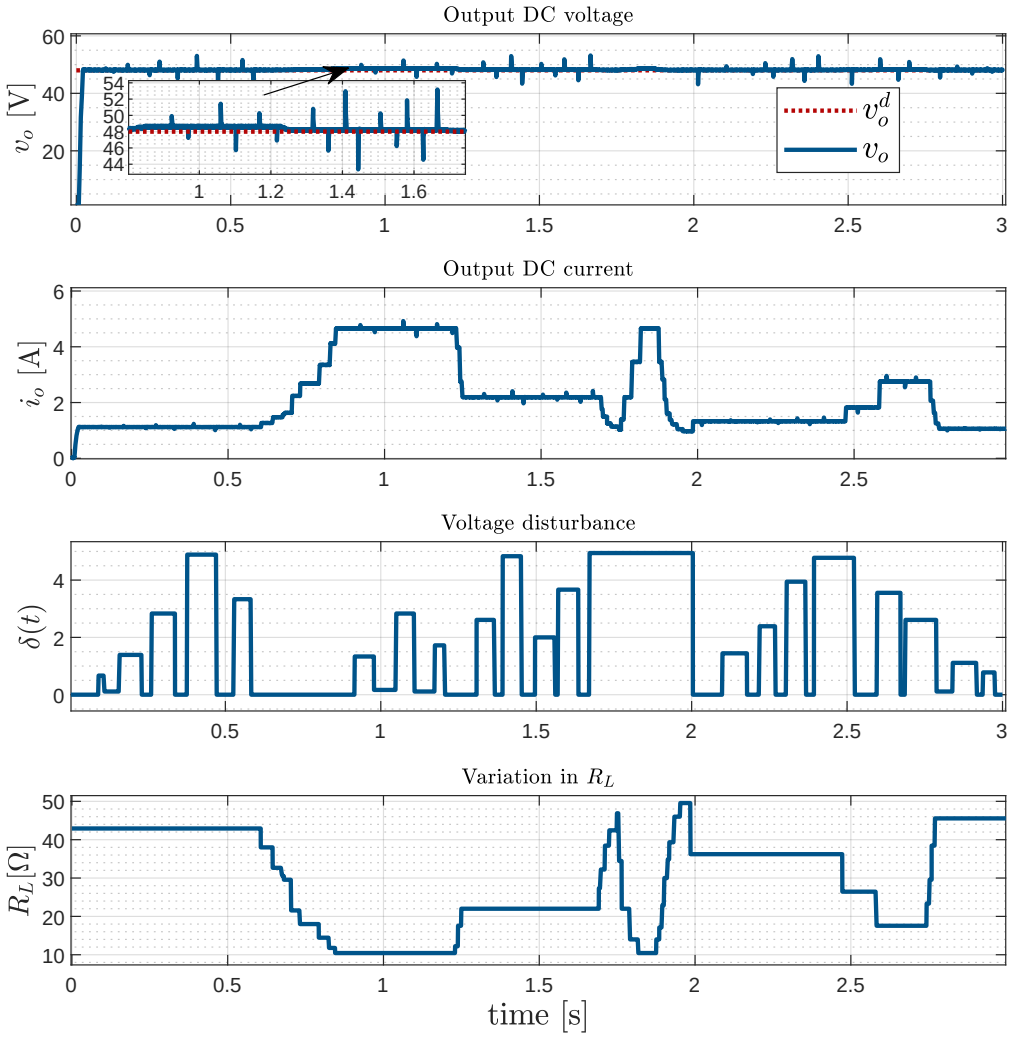

Figure 4.2: Performance of the robust control in finite time. The first graph in blue color shows the calculated v_o value; while in dotted red color the desired v_o^d value. The second graph expresses the output current i_o which follows a tracking of v_o concerning the variation of the load R_L. The convergence time is less than 0.5s. The third and fourth graphs act as perturbations to the system; the third graph is a disturbance in rectifier output. The fourth graphs are variations of R_L around the nominal resistive load.

i_o as a response to the added impulse, regarding the impulse response peaks up to 53 V in the higher magnitude impulses, in i_o the peaks were lower because R_L value was high. Starting at 0.6s the value of R_L began to vary smoothly, starting with a charge of 50 Ω progressively decreasing and then increasing the charge value. During this time no perturbations were added. As an observation during the increase in the value of R_L the voltage v_o was not impaired, while i_o converged to a newly calculated value due to Ohm's law. After 0.6s R_L was maintained at a fixed value of 10Ω in the same way perturbations were added, starting with a magnitude of 5V and ending with 1V. In this case, the response that v_o had was equal to when it had a higher load resistance while the peaks in i_o were higher, this is because the resistance decreased and follows Ohm's law. At 1.2s a 5V step was added and maintained its magnitude until 1.7s, at this instant of time and under the perturbation, R_L increased and decreased from 10 - 40 -10 Ω. the stability of v_o and i_o was not affected under these conditions and as step response only one peak was obtained which immediately converged to its desired value. In the following seconds of the experiment we continued adding perturbations and selecting R_L with different values where the stability of v_o was not affected.

The second point to evaluate in this experiment were the states i_d and i_q. In these plots it is evaluated that the states follow the corresponding desired value, for i_d^d the value calculated with equations (3.32) while i_q^d = 0. The results of these plots were made in the same experiment as the plots in Figure (4.3), whereby the changes in R_L and the impulse response are the same. The results are shown, in blue i_d converges to i_d^d calculated showing a small error; this is because the controller is not designed for variations around the R_L parameter. The same happens for i_q, which converges to zero. From 0 to 0.25s the load was kept fixed, adding perturbations for both states are peak only, in the following seconds when the load is reduced, i_d increases along with its desired preserving or decreasing the error between both, while i_q takes a value close to zero, it should be noted that for this to be fulfilled must make a range in the load that is added.

Finally Figure (4.4) shows the control outputs, the first graph corresponding to p_d and p_q, where the control takes values close to zero to stabilize the system. The lower graph shows the controls transformed into $\alpha - \beta$, this transformation goes to sinusoidal constant values.

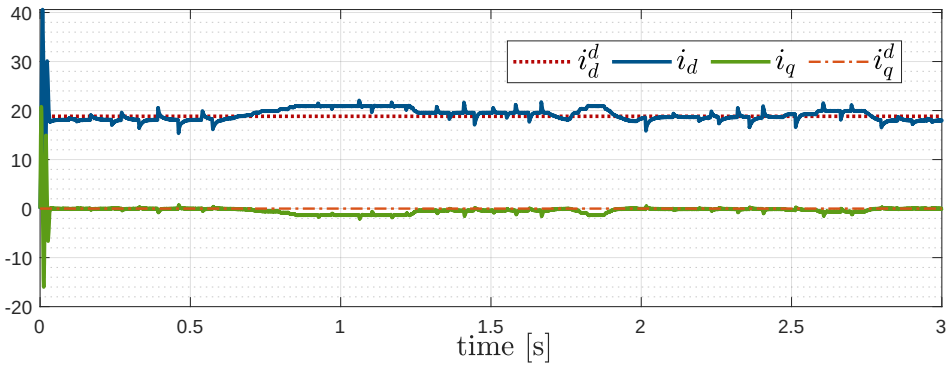

Figure 4.3: The states i_d and i_q, and their desired values. These states converge to their desired values with small transient variations due to the variation of R_L and the perturbation $\delta(t)$. However, the controller succeeds in rejecting these perturbations, and the states achieve convergence. Note that i_q (green color) converges to i_q^d (dashed orange color) with a small error precisely at the time when R_L varies greatly (e.g. during $t = 0.6$ to $t = 2$s). This occurs because the controller is not designed to cope with large variations of the R_L parameter. However, the closed-loop system maintains state convergence and a power factor close to one, as expected.

This control although not designed for an unknown R_L was able to stabilize the system under the added conditions, on the other hand, it should be noted that in the states i_d and i_q the signal becomes noisier and peaks of greater magnitude to have step response.

Adaptive and robust control [Proposition 2]

The second control strategy is the proposed adaptive robust controller, the structure integrating the circuit together with the control (see in Figure 3.2). We started by analyzing the noise response of the system output along with the variation of R_L, these experiments are shown in Figure (4.5). The simulation duration was 3s in which the convergence to v_o^d was less than 0.25s, during a period of 0.5s perturbations was added in which the value of R_L was not varied. During this period the control was optimal against the perturbations, having only 50v peaks, the current i_o following ohm's law reached its calculated value. From 0.6s the value of R_L increased and decreased without contemplating a step as noise, both v_o and i_o behaved as expected, only with i_o converging to their new calculated desired values. during the period of 0. 8 - 1.6s R_L was held fixed while steps were added, due to ohm's law, the peaks in i_o were smaller in scale. from 1.7 to 1.9s a magnitude 5 step was held while R_L decreased and increased, obtaining good control results. Figure (4.6) now

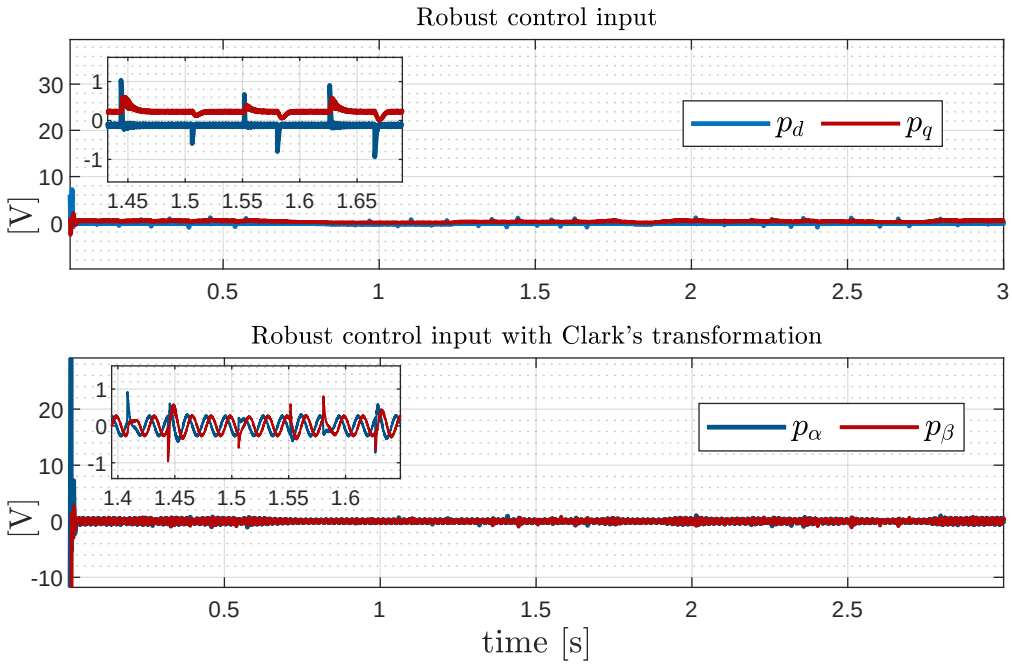

Figure 4.4: The controls p_d (3.26), p_q (3.28) and their transformation α-β (3.45). The upper graph represents the control outputs p_d in blue and p_q in red. In the lower graph, Clark's transformation is applied from which p_α in blue color and in red color p_β is represented. As can be seen, the peaks respond to variation in the parameter R_L and disturbance $\delta(t)$.

shows the i_d i_q states, it can be noticed that the use of this controller reduced the error between the desired values and the state, especially in i_d. Also the response to the step was smaller scale peaks and shorter duration.

The behavior of the states i_d and i_q ,the error between i_d and its desired value has been reduced, the control compensates in the instants that R_L varies. The step response has also improved, the peaks generated are smaller in magnitude and the convergence time is shorter. For i_q the signal always maintains values close to zero in the range that R_L works, the convergence time as a response to the step were reduced as well as the magnitude of the peaks as a response.

Figure (4.7) shows the control outputs p_d and p_q, where the control takes values close to zero to stabilize the system. The control shows different values when some perturbation is added. The lower graph shows the controls transformed to $\alpha - \beta$, this transformation goes to sinusoidal constant values. In these experiments, a better response to the system was obtained by the controller, being the i_d i_q states the ones that improved, because this

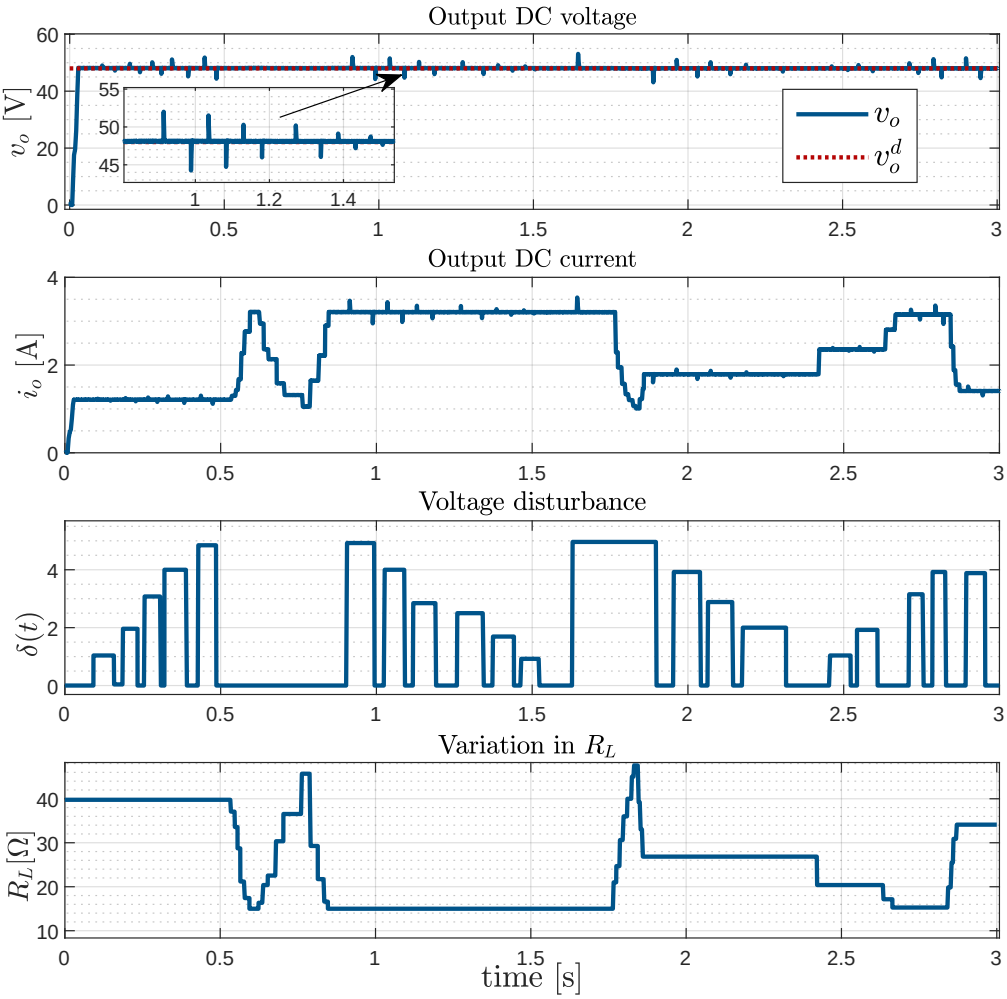

Figure 4.5: The following figure represents the performance of the robust controller with adaptive parts for parameter estimation. The first graph in blue color shows how v_o behaves in the presence of perturbations and converges to v_o^d. The convergence time is less than 0.25s. As shown in the third and fourth graphs, we add step perturbations of different magnitude as well as changes in the value of R_L. The control manages to compensate for these changes and noise in the system, adding perturbations throughout the experiment with a magnitude of 1V and 5V at R_L = 10 - 40Ω. Even so, the control manages to effectively compensate the variation of R_L and external disturbances to the system improving the results that were obtained with the robust control.

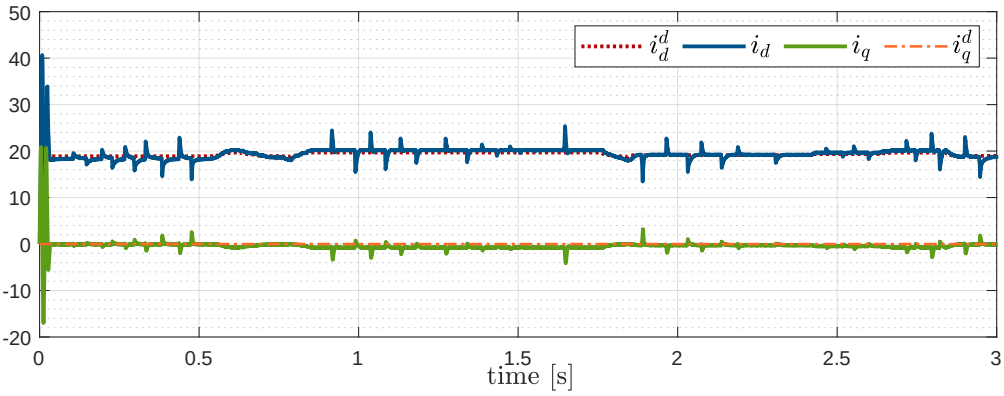

Figure 4.6: The states (i_d,i_q) converge to their desired values. Both signals have small transient peaks due to the $\delta(t)$ disturbance. However, the controller manages to reject these disturbances. i_d is resistant to variations of R_L decreasing the error and computing the value of i_d^d. Note that i_q (green color) converges to i_q^d (dashed orange color) with a slight error. This controller manages to stabilize i_d in addition to maintaining a power factor of one because i_q is kept at zero.

controller does count an unknown R_L and these states are the ones that are more affected by the changes in R_L. For all the states of the system, there was a faster convergence speed in response to the perturbations.

Proportional - integral controller

In this section, a comparison has been made with a PI controller. In order to measure the performance of the above controls. The structure of the controller is shown in the work of [69]. The parameters of the Table 4.1, the following values were selected for controller gains k_p= 2000, k_i =1000, and a simulation time of 3s was considered. The results of the experiment are shown in Figure (4.8). It shows the response of v_o and i_o to the perturbation $\delta(t)$ and the variation around the parameter R_L. It is evident that v_o and i_o never converge, being directly affected by the perturbations and having non-transient responses.

The results of the states (i_d,i_q) are shown in Figure 4.9. It is evident that the control does not converge to the desired value at i_d because this control is not designed to compute the value of i_d^d. Furthermore, it is directly affected by the $\delta(t)$ perturbation and the variation around R_L. i_q manages to remain at a value close to i_q^d = 0 but oscillating too much in response to the $\delta(t)$ perturbation and a high R_L. A second experiment was performed with the following parameters E_m = 40V, R = 0.5Ω, L= 0.01H, C= 1000mF and v_o^d =24V, the

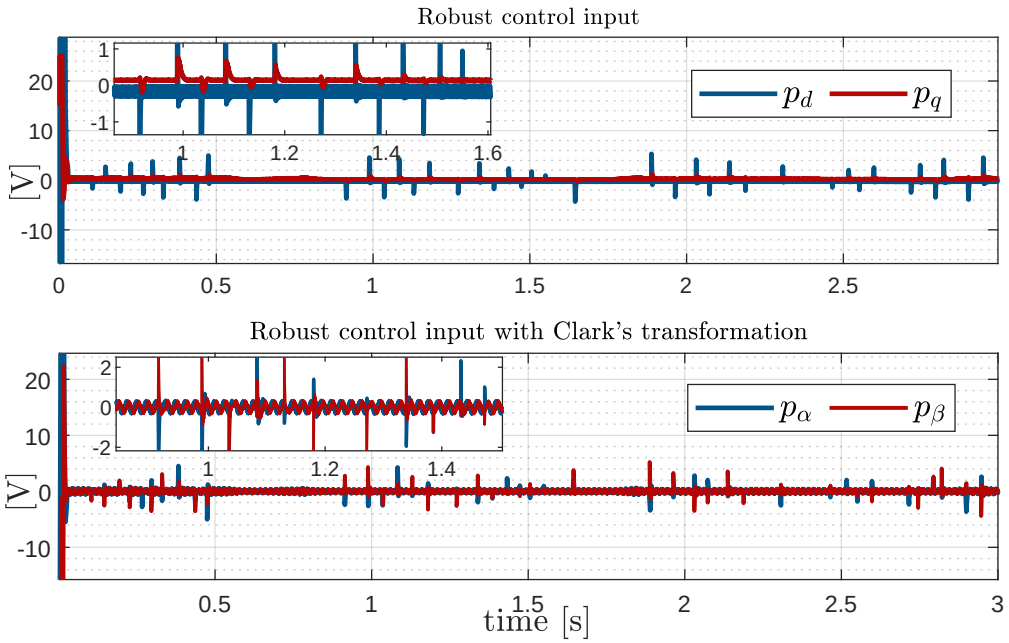

Figure 4.7: The following figure corresponds to the controller outputs and their transformation α-β. The upper graph represents the control outputs p_d in blue and p_q in red. In the lower graph, Clark's transformation is applied from p_α in blue color and in red color p_β is represented. As can be seen, both have the effect of the perturbation. Compared to the robust control, both controllers work at very similar values.

control worked efficiently with a convergence time of 0.2s and was perturbation resistant.

Discussion of the results

According to the tests carried out, the adaptive and robust control gave the best performance. For the i_q state the robust control does not stay at zero, which is crucial to maintain zero power factors. The adaptive robust control showed better performance at i_q since it stays at zero and is also less noisy in the presence of disturbances. In the v_o state, the robust control and the adaptive robust control show very similar performances, similar convergence times but differ in the response to the perturbation because the robust control shows a higher peak magnitude. On the other hand, the PI control shows deficiencies since it did not manage to stabilize the voltage, being the one that showed the worst performance.

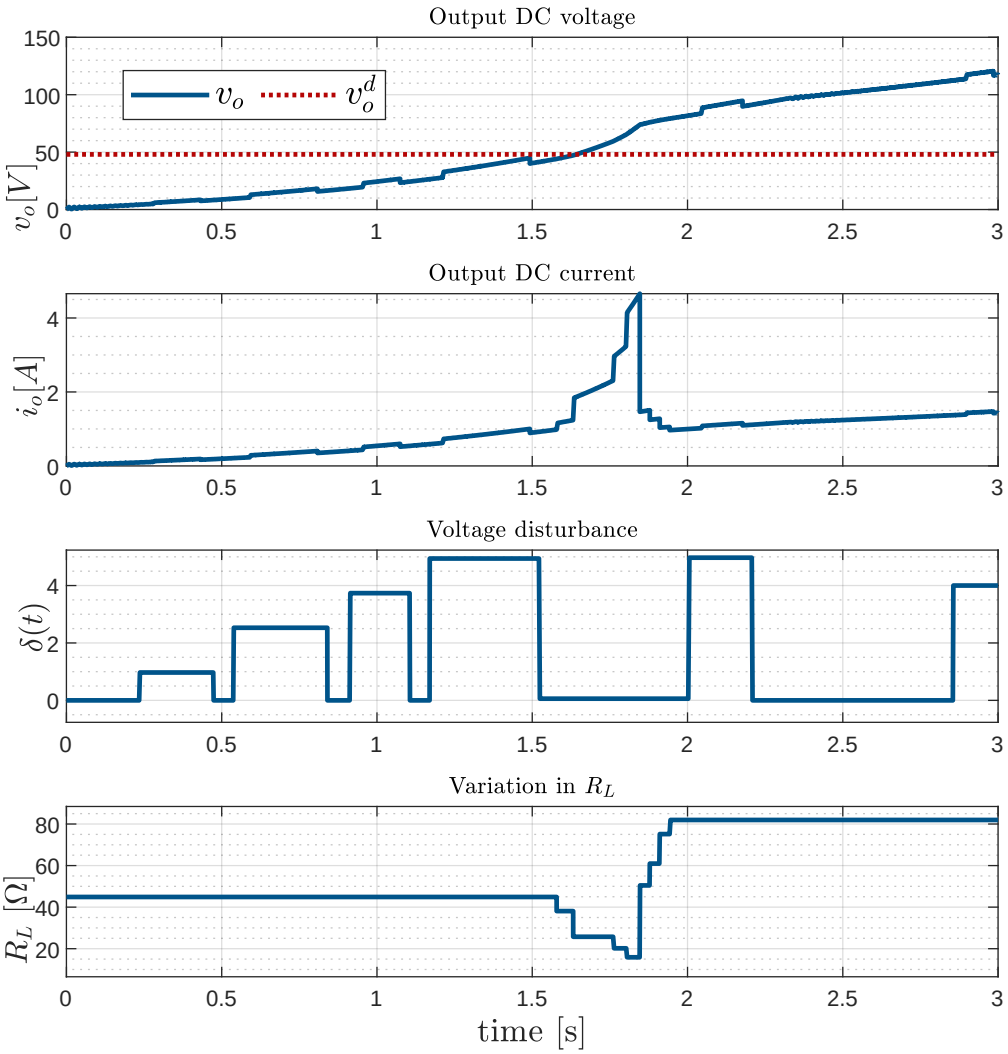

Figure 4.8: The following figure represents the performance of the proportional-integral (PI) control. The first graph shows the state v_o; it never converges to its desired value v_o^d (dashed red color). The output current i_o is shown in the second graph. Both plots show a non-transient response to the $\delta(t)$ perturbation and the variation of R_L. The third and fourth graphs show the disturbance at the rectifier output as well as the variation of the R_L parameter. This controller was not able to stabilize the system with the parameters used.

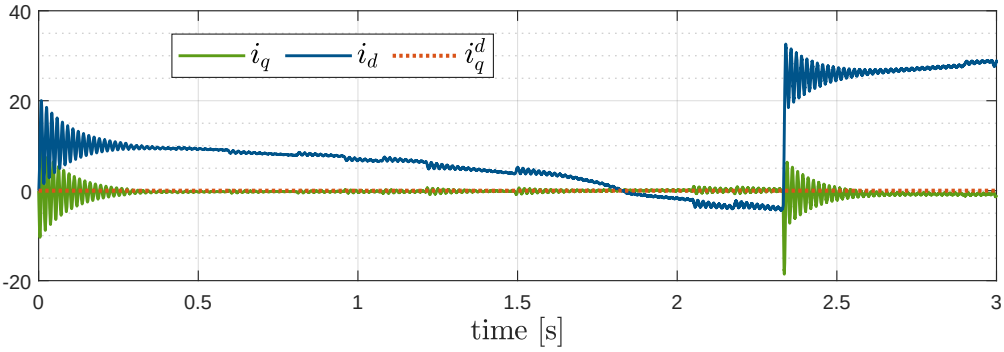

Figure 4.9: The following figure shows the behavior of the states (i_d, i_q). It is highlighted that i_d^d is not computed so i_d does not converge to the desired value. i_q remains at zero, but this is impaired when there is a very large variation around the R_L load.

4.1.2 Software in the loop simulation SITL

In this section, tests are performed to measure the performance of the proposed adaptive nonlinear control of the converter. The experiments were performed using a Pspice-Simulink environment. The analog and power electronics part was performed in capture-OrCAD while the adaptive control was performed in Simulink. APT30G100 IGBT transistors of 30A and 100V, Schottky 120NQ045 rectifier diodes of 120A at 45V were used. The parameters used for the system are listed in the Table 4.2. The adaptive control scheme was implemented in Simulink and packages for Clark and Park's transformation were added, as well as pwm generation using the SVPWM technique. The pwm has a frequency of 10kHz, the converter has a R_L = $45\ \Omega$. At its output an v_o^d = 45 , at the input i_a and e_a a fully sinusoidal shape is sought.

Figure (4.12) shows the rectifier input current and voltage using a pwm control with a predetermined pulse. It can be seen that e_a does not maintain a nominal voltage, while i_a does not have a sinusoidal shape, between the two signals there are lapses in which there is an offset between them, which means power losses. In v_o and i_o it can be seen that both signals do not regulate effectively, having high amplitude oscillations. In both figures, the problems are because control has not yet been implemented, only a pwm signal with a predetermined timing has been used and is not well synchronized as a function of current frequency and amplitude.

In the following test, the same circuit is considered with the same parameters and compo-

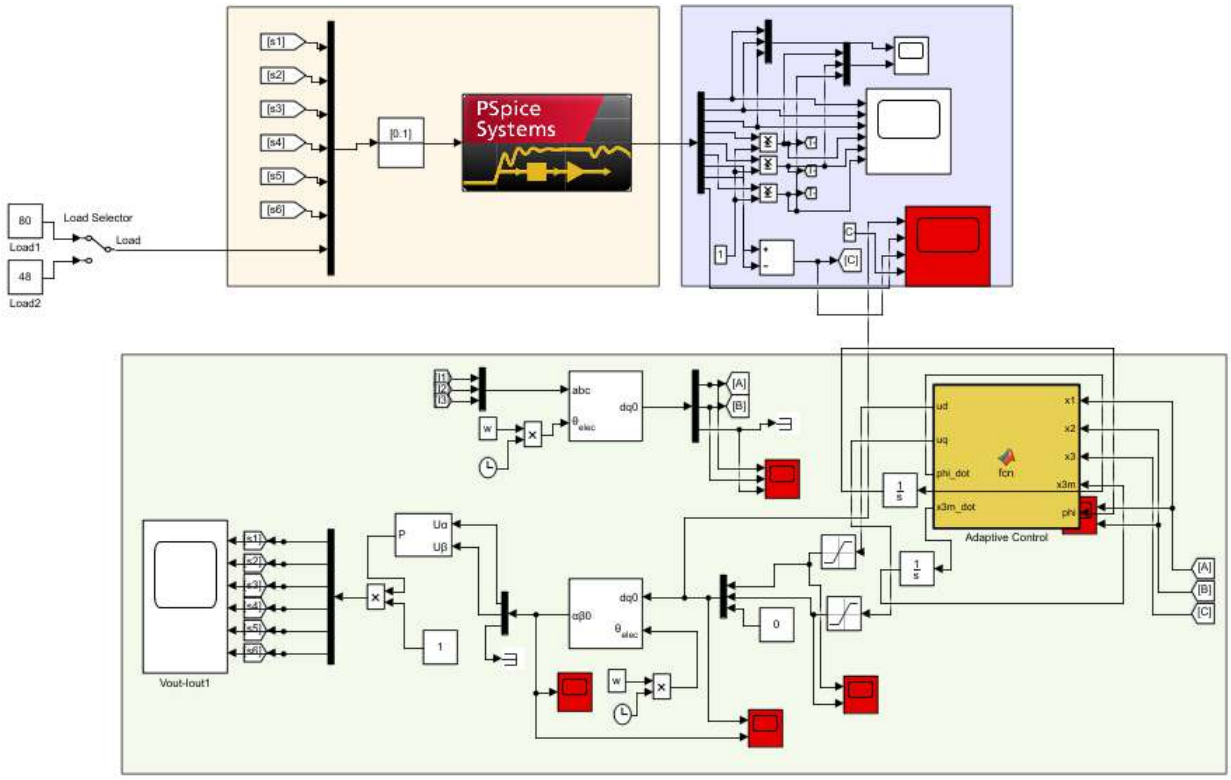

Figure 4.10: Simulation carried out in Simulink. In this simulation, the system or electrical circuit was replaced by a more real one, made in PSpice. In the red block is the circuit that includes the generator and the rectifier.

Table 4.2: Parameters used in SITL of adaptive non linear control

Parameter	Value	Parameter	Value
E_m	$80V$	$k2$	300
L	$5mH$	$k3$	1200
x_3^d	$48V$	a_m	300
C	$8000\mu f$	b_m	300
ω	$60H_z$	u_m	equation (3.36)
R	0.1Ω	γ	1
R_l	80Ω	k_m	300
pwm amplitude	5	$Diode$	120NQ045
pwm frequency	$10kHz$	IGBT	APT30G100

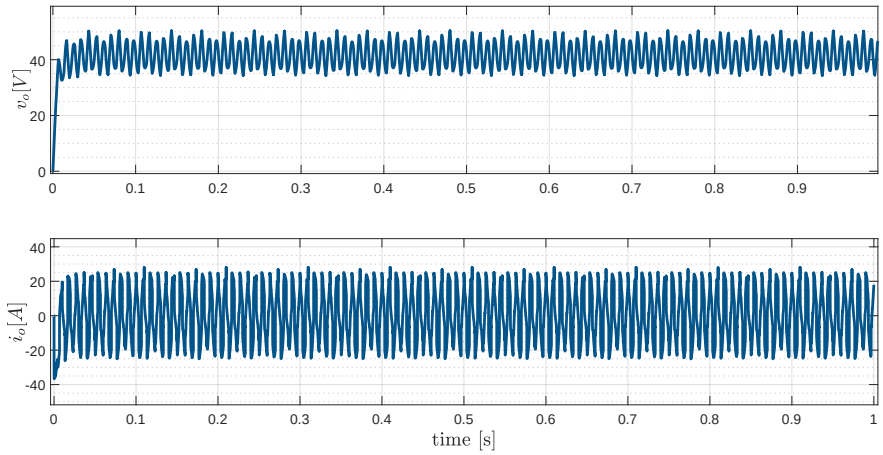

Figure 4.11: The upper graph shows v_o using the SITL circuit while the lower graph represents i_o. Both plots are without the implementation of any control to regulate them.

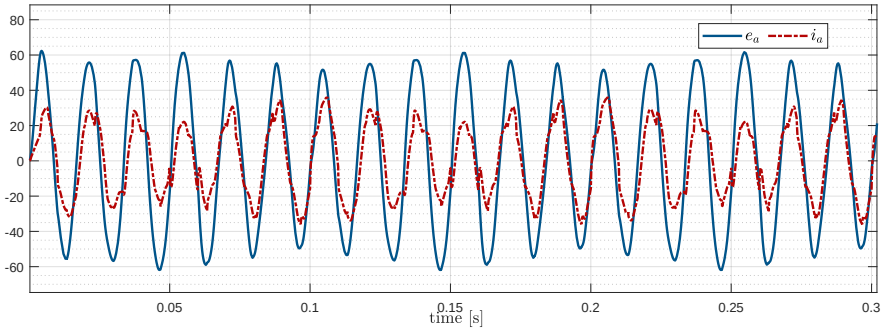

Figure 4.12: The input voltage e_a and current i_a of the circuit used in the SITL. i_a has distortion and its magnitude as with e_a changes and does not remain at a fixed value, in some instants i_a is not completely in phase with e_a, which affects to maintain power factors close to one.

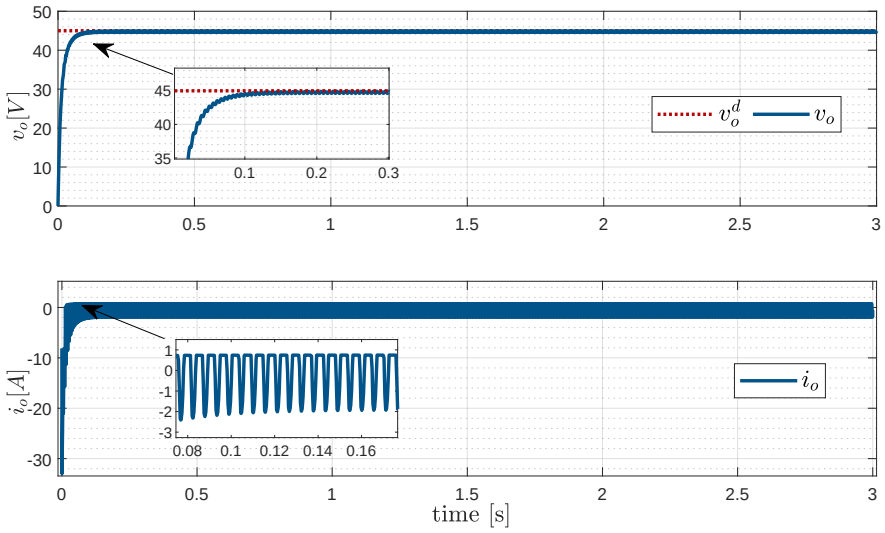

Figure 4.13: The upper graph represents the behavior of v_o. The blue color shows the state v_o and the red color shows the setpoint v_o^d. The system has a fast convergence time of less than 0, 25s. The lower graph represents the behavior of the current i_o without perturbation, as mentioned this is not regulated but controlled and has more noise.

nents, the pwm control is replaced by the adaptive robust control. Figure (4.14) shows the signals (e_a, i_a) with the control implementation, both signals show a fully sinusoidal shape and they are fully in phase, which means good power performance. The states (i_d,i_q) are shown in Figure (4.15). They still manage to converge to their desired value, unlike the first simulation tests, which have more noise.

Now in figure (4.13) we show v_o and i_o. In the graph, above you can see that v_o has a very fast convergence time that converges smoothly and without oscillations, the same happens for i_o. For the case of i_o, because it does not have any perturbation always maintains the same current, this is too noisy and oscillates from 1 to -2 A. In the Figure (4.16) the control signals are shown, both graphs show the expected behaviors, and likewise, the values in what is working is from 1 to 0. For p_α and p_β it has the expected oscillations due to the Clark´s transformation. In Figure (4.17) and (4.18), the pwm signal to be distributed to each actuator can be better visualized. Each line has two actuators that do not remain open at the same time so six pwm signals are being one the negation of its pair having s_i and its negation $\bar{s}_i$.

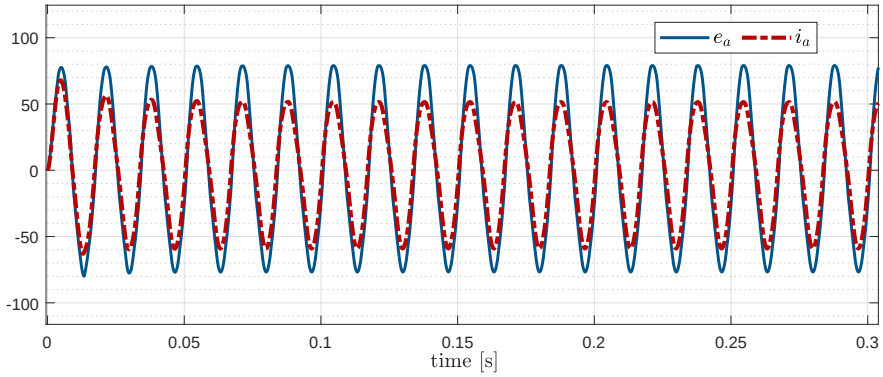

Figure 4.14: The following figure represents e_a and i_a of the SITL and with the application of the adaptive control, in red color, i_a is shown which no longer contains distortions. In blue color e_a shows that e_a maintains a fixed voltage. Both signals are in phase, indicating a power factor equal to 1 or very close to 1.

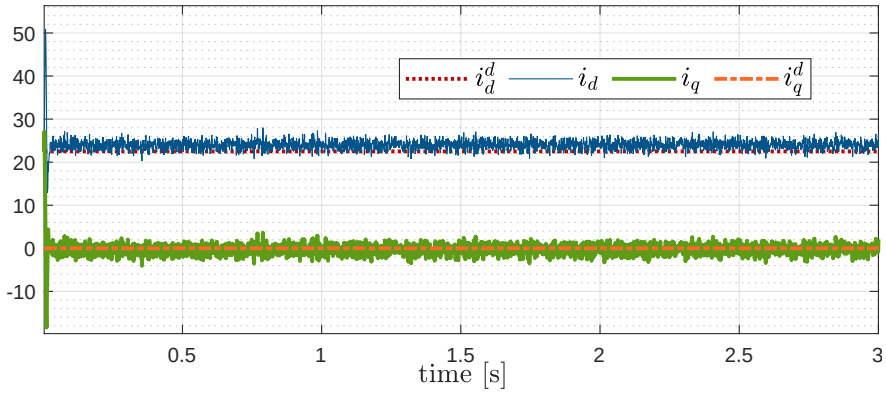

Figure 4.15: The states i_d and i_q were able to stabilize at the desired values, while i_d converges to i_d^d with a slight error. For i_q the same thing happens, it maintains its stability and converges to zero.

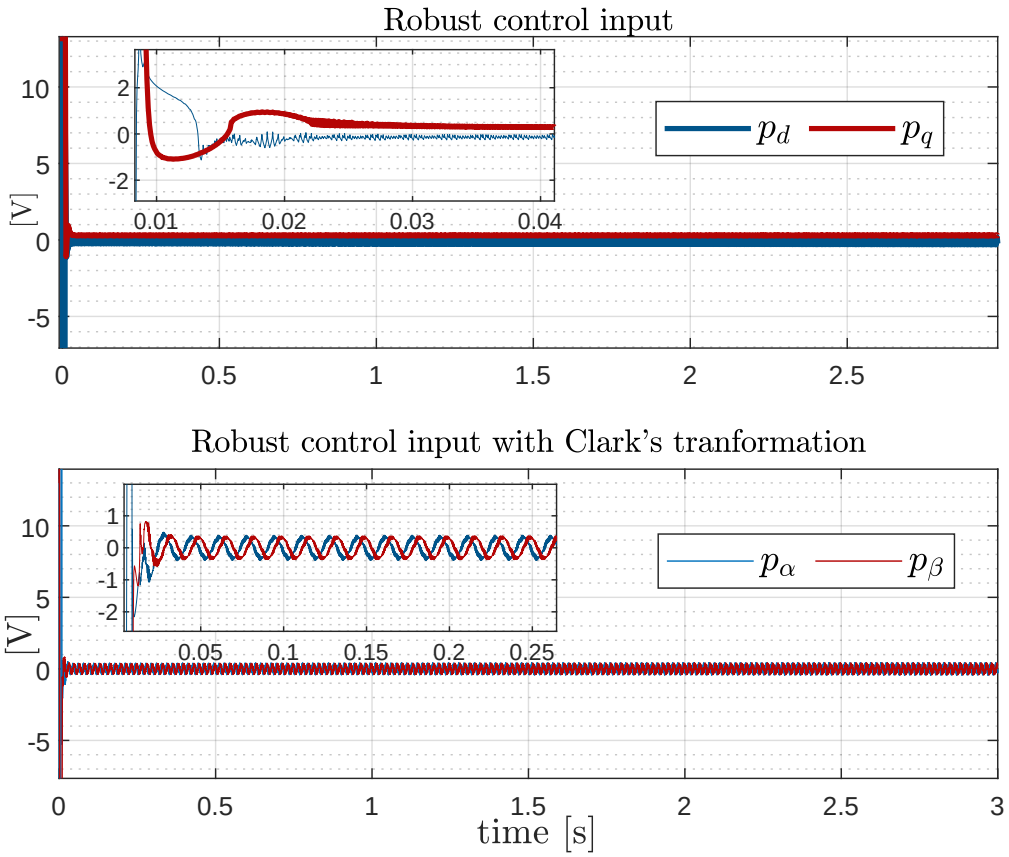

Figure 4.16: The upper graph represents the p_{dq} control while the lower graph in its p_α - p_β form by means of the clark transform. Black p_α and red p_β.

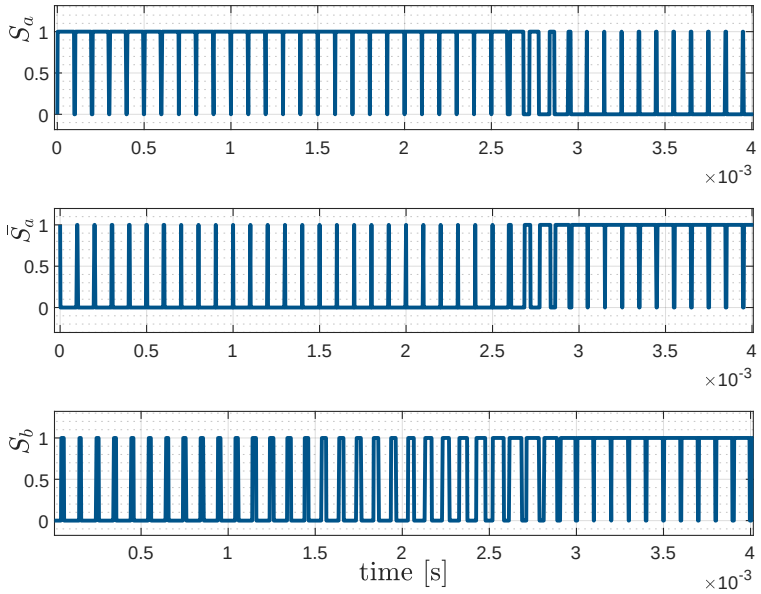

Figure 4.17: Pulse width modulation generated with the SVPWM technique. S_i and $\bar{S}_i$ cannot be open at the same time, which is why $\bar{S}_i$ is the negation of the S_i signal.

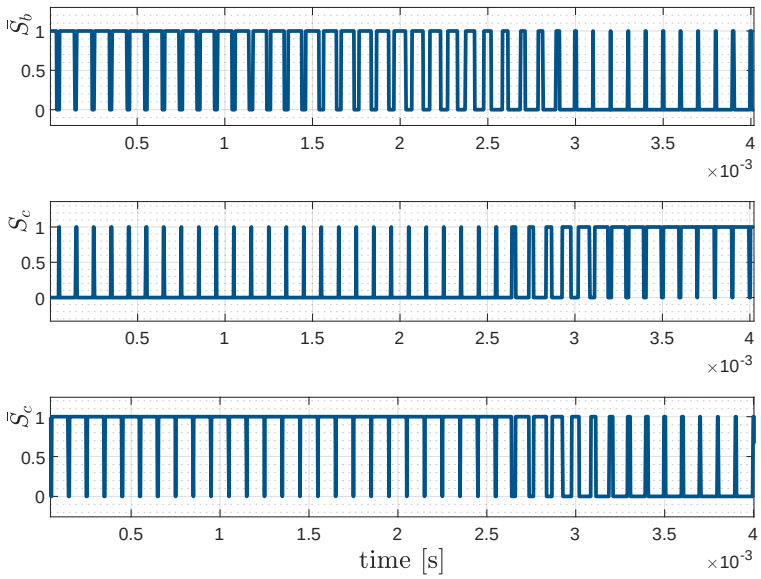

Figure 4.18: Pulse width modulation generated with the SVPWM technique. S_i and $\bar{S}_i$ cannot be open at the same time, which is why $\bar{S}_i$ is the negation of the S_i signal.

Discussion of SITL results

The simulation showed that it is necessary to implement control or to have a synchronized pwm signal for the three-phase rectifier to work properly. In the graphs corresponding to the PSpice environment, it is evident that it requires some calibration or adjustment in the pwm triggering. The graphs corresponding to the adaptive robust control showed a better performance in the states, there were improvements in the output voltage v_o having a non-noisy signal and converging to the desired value. In addition, at the input of the rectifier both current and voltage are in phase with a totally sinusoidal shape.

4.2 Advances in platform

This section presents the progress made in the construction of the platform. It begins with the construction of the generator, which integrates the combustion engine and the brushless motor. The points that were considered for its construction, especially for a quad-rotor, are discussed, followed by the CAD design of the platform and finally with its construction. Afterward, the design of the power electronics is approached, in this case, we started with an uncontrolled three-phase rectifier, its simulation and real experiments are presented.

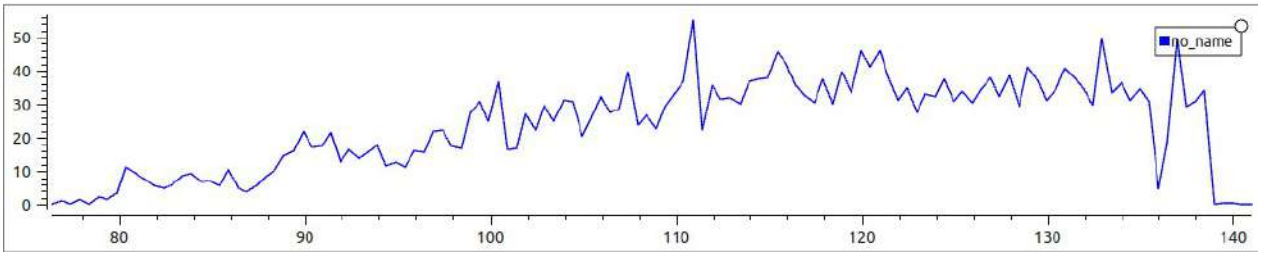

Figure 4.19: Current characterization obtained from the flight of a quadrotor in different flight modes.

Generator. Design and construction

Characterization of a quadrotor for the design of the generator it is essential to know the power that it will have to be able to supply, the graphs that represent the dynamics of the current and the voltage of a quadrotor are obtained, this is integrated by 4 motors of 420 KV and uses a lithium-polymer battery of 24 V of 10000 mA of discharge. The Figure (4.19) shows the dynamics of the current where the Y axis represents the amperage and the X axis the time, it can be shown that it has an average amperage of 40 A, but it usually has peaks of up to 50-60 A, these peaks depend on weather conditions, flight modes and the pilot's skill to handle the vehicle. The Figure (4.20) represents the voltage dynamics, this voltage is the one that counts each cell of the battery (4.5V), from it we can obtain that this vehicle under this condition has a flight duration of 14 minutes, a battery having a cell with a voltage lower than 3.8 can be risky since its life cycle is damaged or catch fire. For the design of the generator of this vehicle an amperage was taken considering a margin of the peak (70 A) and the 24 V that the vehicle requires. Multiplying the amperage and the voltage it is obtained that the generator must supply at least 1.6 kW, if an amperage of 60 A of 1.5 kW is considered.

The generator design was contemplated for a 1.6 kW quadrotor, the brushless motor, as well as the internal combustion engine, were selected to be able to produce the required power. The power electronics, on the other hand, were designed to support the generated power as well as to minimize power loss as much as possible.

Figure (4.22) shows the CAD design of the first proposed prototype, which is composed of three subsystems: electromechanical, electronic, and control. The electromechanical

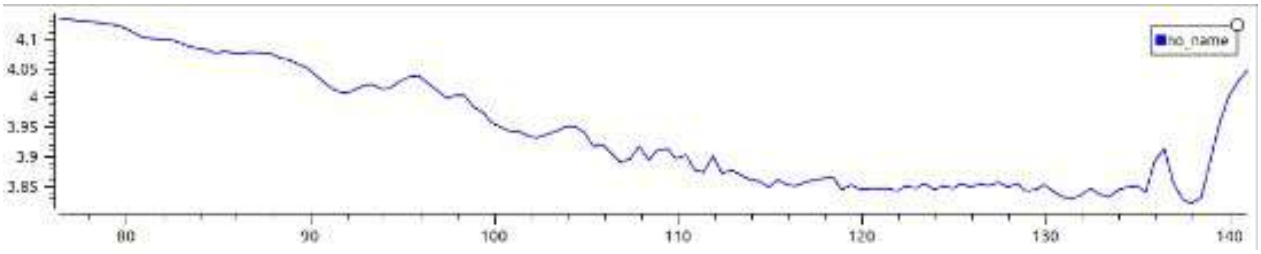

Figure 4.20: Characterization of the voltage and discharge of a 5-cell LiPo battery of a quadrotor in different flight modes. The graph shows the voltage of one cell of the battery and the time it took to discharge, which was 15 minutes.

system is composed of a 2HP traxxas motor giving the best performance at 3000 - 4000 RPM. On the other hand, the brushless motor used is a U8 of the brand U8 lite of 100 KV, in the Figure (4.21) the performance of this motor is shown. It can be seen that the point where it has the best performance is at 2000 rpm, but with a power capacity of 150 W at 3500 rpm it has a performance of 76% but with a capacity to produce 1350W. The other sub-system is the three-phase controlled rectifier, which was designed to withstand the power input to the rectifier. In this case, the IGBT transistors with Schottky diodes AFGHL75T65SQDC were used and a 2200 and 2500 uF capacitor was used to filter the output.

In this first design a 1:3 reduction had been added (see in Figure 4.23) because a combustion engine with a higher number of revolutions had been selected, so to be able to couple to the electric motor, the speed had to be reduced and the torque increased, with the components mentioned above this design was omitted and a direct coupling was chosen.

Finally in the Figure (4.24) shows the mini-generator construction, this is already integrated with a dc motor to start the combustion engine, a filter was added in the carburetor to filter dust particles and do not mix with the fuel that cause the ducts are clogged, Also a servomotor was added to control the fuel opening, this is essential to control the revolutions of the combustion engine, now considering that this generator will be varying its altitude this directly affects the stoichiometric mixture, which makes it have more or less RPM. In this design, both engines were directly coupled. In orange color is the three-phase rectifier, as can be seen, this is somewhat spacious, due to the addition of disciples in the IGBT

Figure 4.21: Efficiency, power, current and RPM graph of the T-motor U8 brushless motor. These graphs are provided by the manufacturer.

and decrease power losses.

4.2.1 Experiments in platform

Non controlled rectifier

Specific tests were performed in the rectification stage. A total of three rectifiers were built, the first was an uncontrolled three-phase rectifier, the second was a controlled three-phase rectifier for low power, and the third was the rectifier circuit to be used by the generator. The first circuits are currently being tested. For this purpose, a test bench was built consisting of two coupled brush motors, which simulate the three-phase generator. It should be noted that this test rig is for no-load systems only. Figure (4.25a) shows the designed test bench, in which a non controlled rectifier was tested. This is composed of a 780KV brushless motor that transmits mechanical energy, because the higher the KV, the higher the number of revolutions it delivers. The next motor was a 450 KV brushless motor considering that the lower the KV, the more torque the motor delivers. An open-loop control was

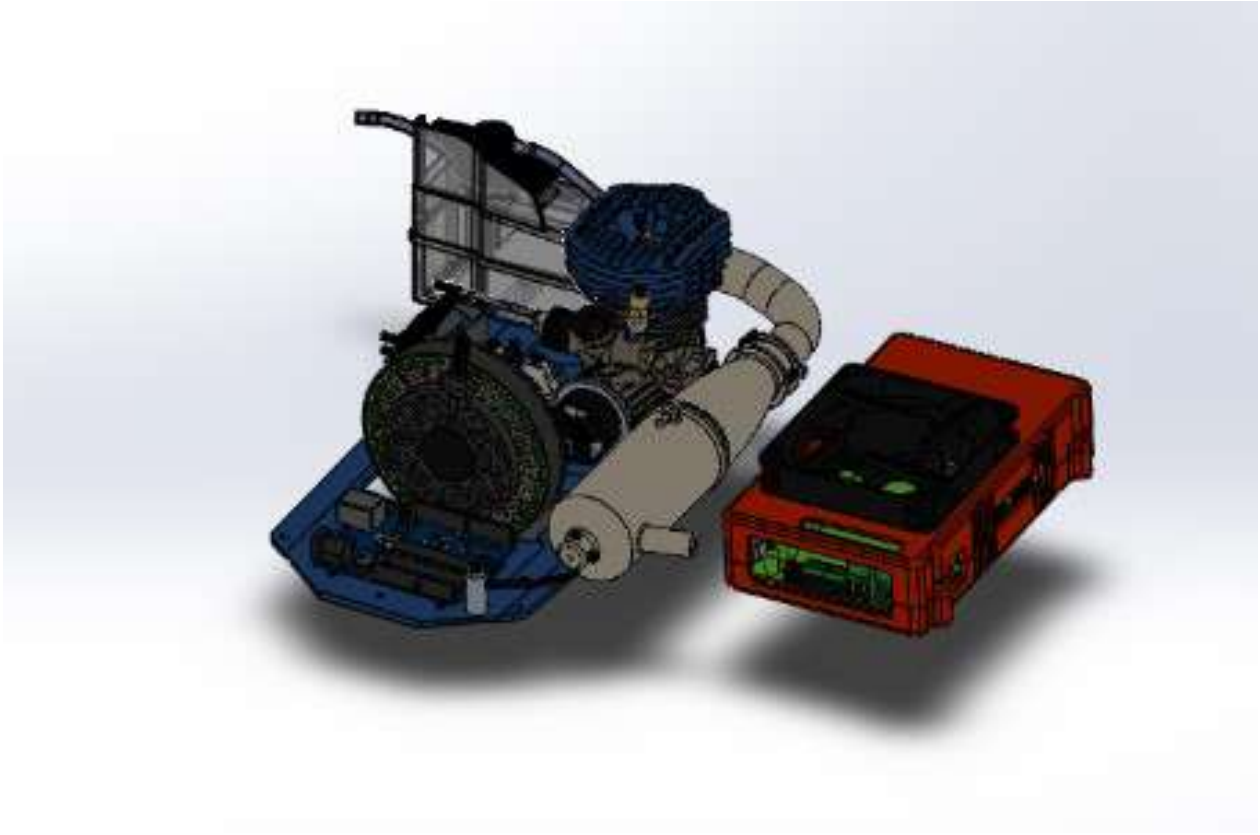

Figure 4.22: CAD design of the proposed platform is integrated for two-stroke servo-controlled combustion engine which will be in charge of producing the mechanical energy. Brushless motor of 100 kV, in charge of converting mechanical energy into electrical energy. Controlled three-phase rectifier, in charge of rectifying, regulating, and filtering the voltage and maintaining power factors close to 1.

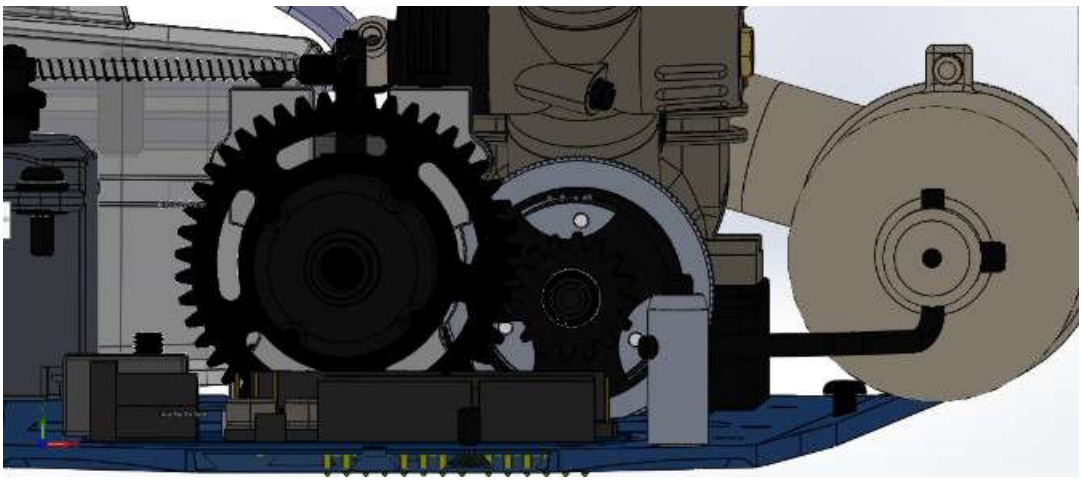

Figure 4.23: First CAD design, the first design had considered a 1:3 reduction due to a brushless motor with lower RPM. This design was considered due to the constant problems that a geared mechanism could cause.

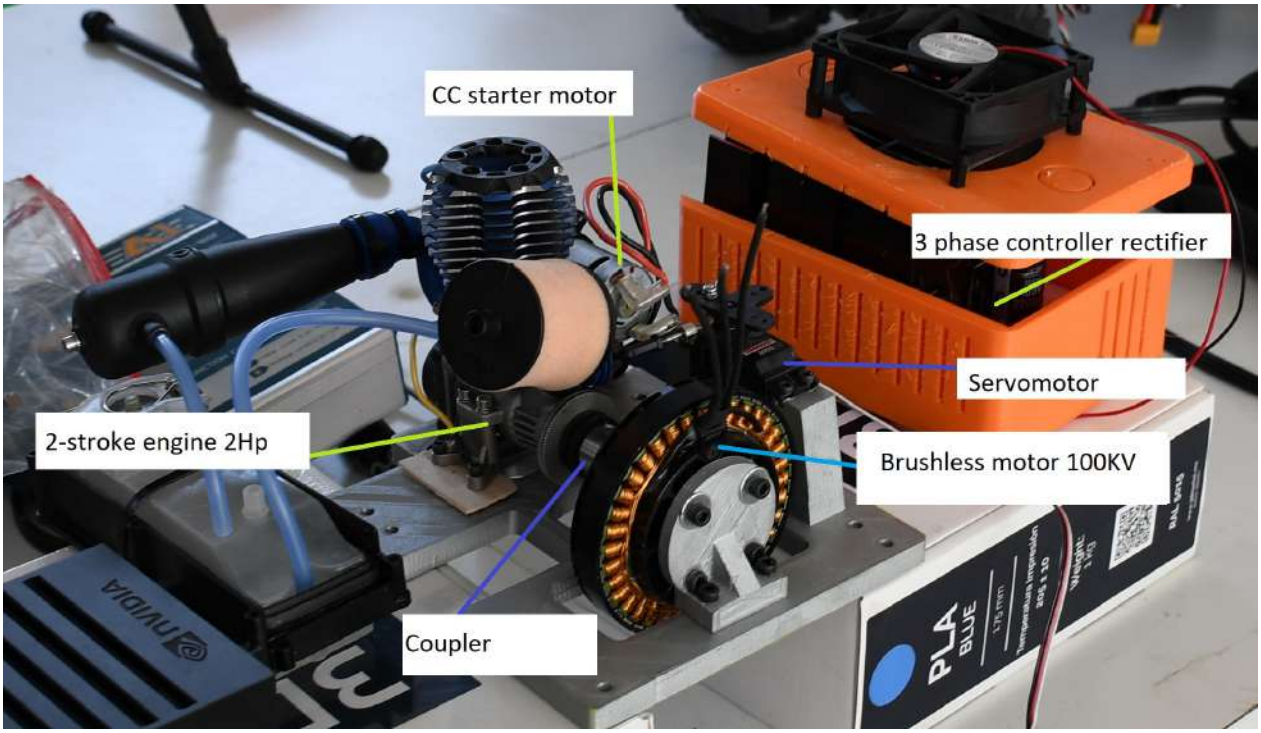

Figure 4.24: Construction of the prototype of the electric mini-generator, in this one we selected the Traxxas brushless motor of 2Hp of 2 times, brushless motor U8 T-motor of 100 KV, three-phase rectifier with IGBT transistors with Schottky diode AFGHL75T65SQDC, capacitor of 2200-2500 uf.

implemented to control the revolutions of the brushless motor transmitting the mechanical energy.

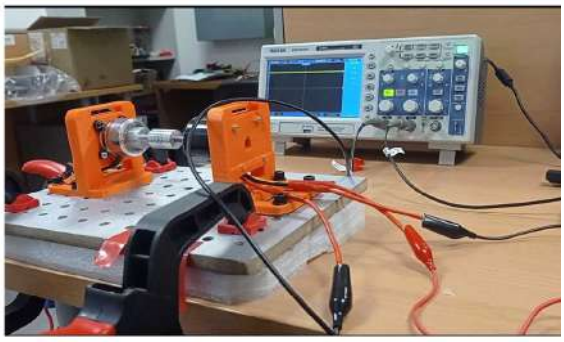

(a) Test bench to test the rectifier stage. In this test bench we used two brushless motors with the capacity to produce the necessary voltage for a quadrotor, this test bench is to test the rectifiers without ”load” for the tests with load will be performed with the combustion engine.

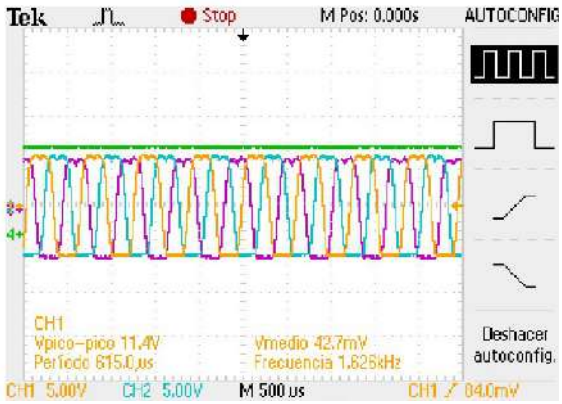

(b) Graph of the experiment show the three phases and in green color the rectified signal, in this test the performance of the rectifier and the voltage produced by the brushless motor were evaluated.

Figure 4.25: An uncontrolled three-phase rectifier was tested on a test bench in order to measure its performance.

The circuit was composed of a driver to control the speed of the motor as well as a radio receiver to operate through radio to control the revolutions of the motor. The speed was increased progressively in order not to damage both motors. The voltage limit is delivered by the generator. The generator supplied a voltage in the range of 5-8 V, due to the rectification stage the voltage obtained was from 8.5 to 13.2V. Since it was not tested with any load, the effect that the load has on the acquired signal is not shown. In the Figure (4.25b) is displayed both the rectifier input voltage that corresponds to each phase of the generator. Although no load was added, each phase does not have a sinusoidal shape and has some distortions, as mentioned above this is since uncontrolled rectifiers are harmonic generators. On the other hand, the acquired output signal does not show any distortion, a series of capacitors totaling 3300uf was used.

Controlled rectifier

Figure (4.26a) shows the controlled rectifier designed in PSpice, then printed and assembled as shown in Figure (4.24). It began with familiarizing in the implementation of control algorithms of physical form, began with the sinusoidal pwm, which consists of adding a triangular signal and a sinusoidal, in the Figure (4.26b) shows an analog circuit composed of operational amplifiers, one is responsible for generating the triangular signal, while the others compare the sinusoidal signal (can be voltage or current) with the triangular, the Figure (4.26) shows the results given by the technique.

Finally, a test was performed with a digital SPWM. The algorithm was loaded into the Arduino MEGA board by first loading it into the proteus software to avoid damage to the equipment or circuitry. The purpose of this test was to generate a PWM signal and become familiar with these algorithms. Figure (4.27a) shows the circuit used in proteus as well as the board used. The results are shown in the Figure (4.27b) in which the output voltage given by the circuit is displayed in green. The signal is noisy and does not remain constant. The script was then loaded onto a physical card. Figure (4.28) shows the capture of the signal obtained from the oscilloscope, where the signal is different from the simulation in this case is noisier and there are times when the signal is not completely square. Finally, although it was not performed in this work, this algorithm will be tested in the following designed boards(see in Figure 4.28a).

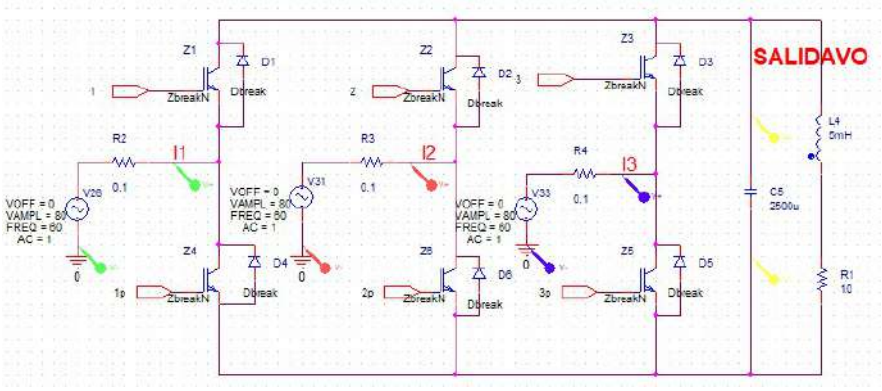

(a) Controlled rectifier schematic using Orcad/PSpice simulation software.

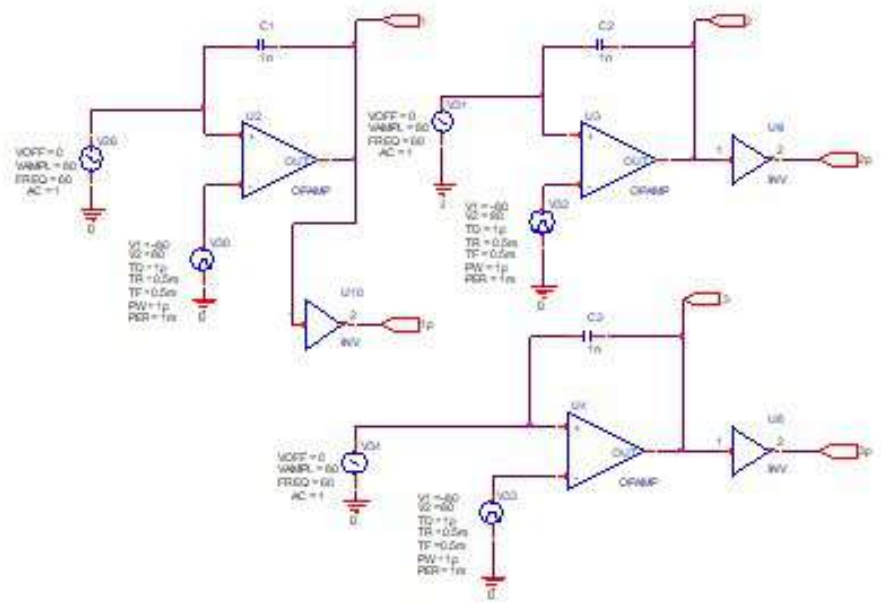

(b) Analog circuit for pwm generation by means of the sinusoidal pwm SPWM technique. This circuit was made for the rectifier circuit to work in Pspice, later it was replaced by the adaptive robust control with SVPWM.

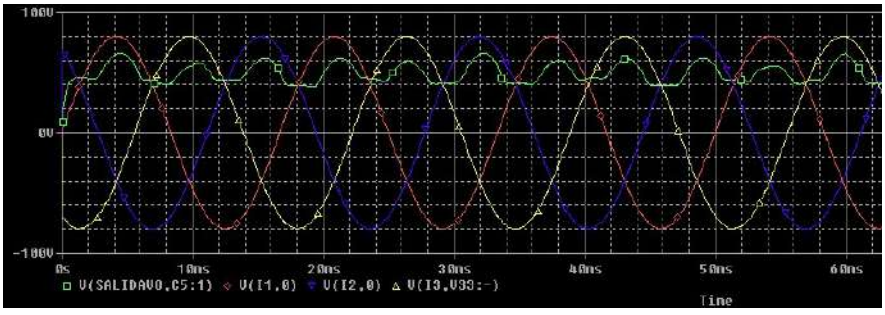

(c) Simulation results using an analog spwm

Figure 4.26: A simulation of a controlled three-phase rectifier was made in pspice, this simulation was then treated to print the circuit and assembled.

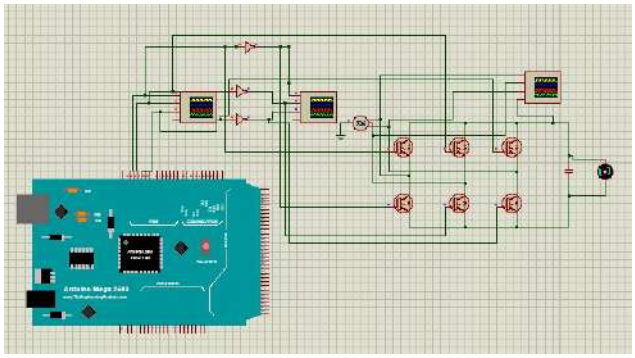

(a) Simulation in proteus of an arduino Mega with script to generate a pwm signal by the spwm technique.

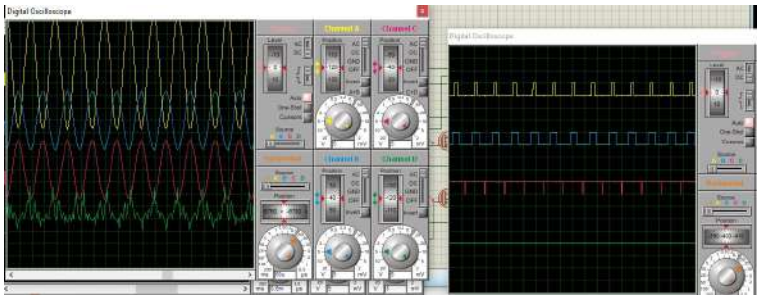

(b) Rectifier results with implemented pwm.

Figure 4.27: Simulation performed in proteus, whose objective was to test a pwm generation script using the spwm technique.

(a) Controlled three-phase rectifiers designed for different tests.

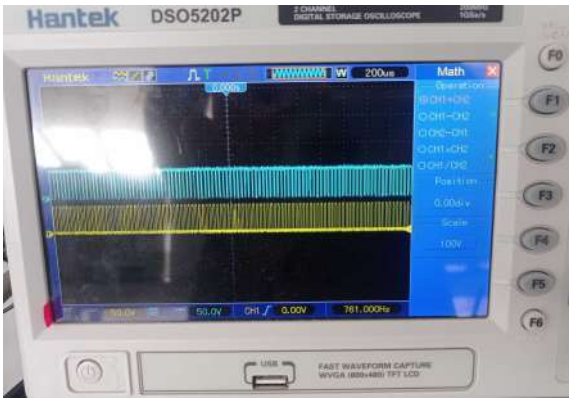

(b) pwm signal acquired from the implemented script.

Figure 4.28: A physical test was carried out to visualize the pwm obtained with the spwm algorithm, and then tests will be carried out with the circuits.

CHAPTER 5

Conclusion

The main part of this work was to model a controlled three-phase rectifier and to propose a control algorithm for voltage and current regulation, as well as to maintain power factors close to one. According to the results obtained in the experimental part, the designed control fulfilled the tasks of voltage regulation, in addition to control the states i_d active current i_q, because i_q converged to zero, it kept values close to 1 in power factor. Now as shown in the SITL simulation in the phase diagram between current and voltage the two remained in phase, indicating that they have power factors close to one. The other point of this work and not less important was the construction of a first prototype of a three-phase mini-generator, according to the results this was designed considering the demand of voltage and current of a quadrotor, the components that integrate it were selected especially to the requirements of the system to which they will be annexed. Previous tests in the design of three-phase rectifiers were carried out, an uncontrolled and a controlled rectifier were designed, for the moment only tests were carried out with the uncontrolled rectifier.

5.1 Recommendations

For future work, the control algorithm will be implemented on a controller board and hardware in the loop simulation will be performed. Subsequently, real-world testing of the controller with the three-phase rectifier will be performed. The electronics will be implemented in the generator. Speed control for the internal combustion engine will be proposed and then testing will be performed. In this work, there was a strong focus on theoretical development, which developed a robust adaptive control. Since there is a few states of the art of adaptive controllers applied to controlled rectifiers and even less implemented physically, there is a scientific contribution to pursue a Ph.D.

Bibliography

[1] G. J. Ducard and M. Allenspach, “Review of designs and flight control techniques of hybrid and convertible vtol uavs,” *Aerospace Science and Technology*, vol. 118, p. 107035, 2021. [Online]. Available: https://www.sciencedirect.com/science/article/pii/S1270963821005459

[2] K. W. Y. L. Xiaodong Zhang, Xiaoli Li, “A survey of modelling and identification of quadrotor robot,” *Abstract and applied Analysis*, pp. 1–17, 2014.

[3] Y. Li and C. Liu, “Applications of multirotor drone technologies in construction management,” *International Journal of Construction Management*, vol. 19, no. 5, pp. 401–412, 2019. [Online]. Available: https://doi.org/10.1080/15623599.2018.1452101

[4] N. Delavarpour, C. Koparan, J. Nowatzki, S. Bajwa, and X. Sun, “A technical study on uav characteristics for precision agriculture applications and associated practical challenges,” *Remote Sensing*, vol. 13, no. 6, 2021. [Online]. Available: https://www.mdpi.com/2072-4292/13/6/1204

[5] S. Montambault, J. Beaudry, K. Toussaint, and N. Pouliot, “On the application of vtol uavs to the inspection of power utility assets,” in *2010 1st International Conference on Applied Robotics for the Power Industry*, 2010, pp. 1–7.

[6] D. Perroud, “Wingtraone gen ii - mapping drone for high-accuracy aerial surveys,” Nov 2021. [Online]. Available: https://wingtra.com/mapping-drone-wingtraone/

[7] “Skyeye.” [Online]. Available: https://www.elevonx.com/solutions/skyeye/

[8] X.-G. Yang, T. Liu, S. Ge, E. Rountree, and C.-Y. Wang, “Challenges and key requirements of batteries for electric vertical takeoff and landing aircraft,” *Joule*, vol. 5, no. 7, pp. 1644–1659, 2021. [Online]. Available: https://www.sciencedirect.com/science/article/pii/S2542435121002051

[9] X. Zhu, Z. Guo, and Z. Hou, “Solar-powered airplanes: A historical perspective and future challenges,” *Progress in Aerospace Sciences*, vol. 71, pp. 36–53, 2014. [Online]. Available: https://www.sciencedirect.com/science/article/pii/S0376042114000633

[10] “Silicon solar cells with screen-printed front side metallization exceeding 19 percent efficiency,” Sep 7AD. [Online]. Available: http://publica.fraunhofer.de/documents/N-73521.html

[11] N. Kingry, L. Towers, Y.-C. Liu, Y. Zu, Y. Wang, B. Staheli, Y. Katagiri, S. Cook, and R. Dai, “Design, modeling and control of a solar-powered quadcopter,” in *2018 IEEE International Conference on Robotics and Automation (ICRA)*, 2018, p. 1253.

[12] T. S Alderete, “Simulator aero model implementation,” 05 2018.

[13] O. Montagnier and L. Bovet, “Optimisation of a solar-powered high altitude long endurance uav with composite wings,” in *Proceedings of the 3rd EUropean Conference for AeroSpace Sciences*, Paris, France, 2009. [Online]. Available: https://hal.archives-ouvertes.fr/hal-01315481

[14] S. Morton, R. D’Sa, and N. Papanikolopoulos, “Solar powered uav: Design and experiments,” in *2015 IEEE/RSJ International Conference on Intelligent Robots and Systems (IROS)*, 2015, pp. 2460–2466.

[15] P. MacCready, P. Lissaman, W. Morgan, and J. Burke, “Sun-powered aircraft designs,” *Journal of Aircraft*, vol. 20, no. 6, pp. 487–493, 1983. [Online]. Available: https://doi.org/10.2514/3.44898

[16] X. Zhu, Z. Guo, and Z. Hou, “Solar-powered airplanes: A historical perspective and future challenges,” *Progress in Aerospace Sciences*, vol. 71, pp. 36–53, 2014. [Online]. Available: https://www.sciencedirect.com/science/article/pii/S0376042114000633

[17] R. D’Sa, D. Jenson, T. Henderson, J. Kilian, B. Schulz, M. Calvert, T. Heller, and N. Papanikolopoulos, “Suav:q - an improved design for a transformable solar-powered uav,” in *2016 IEEE/RSJ International Conference on Intelligent Robots and Systems (IROS)*, 2016, pp. 1609–1615.

[18] R. D’Sa, T. Henderson, D. Jenson, M. Calvert, T. Heller, B. Schulz, J. Kilian, and N. Papanikolopoulos, “Design and experiments for a transformable solar-uav,” in *2017 IEEE International Conference on Robotics and Automation (ICRA)*, 2017, pp. 3917–3923.

[19] A. Noth, S. Bouabdallah, S. Michaud, R. Siegwart, and W. Engel, “Sky-sailor design of an autonomous solar powered martian airplane,” in *Proceedings of the 8th ESA Workshop on Advanced Space Technologies for Robotics and Automation (ASTRA 2004) ESTEC, Noordwijk, The Netherlands, November 2-4, 2004*. Noordwijk: European Space Research and Technology Centre (ESTEC), 2004, pp. F–03.

[20] N. Kingry, L. Towers, Y.-C. Liu, Y. Zu, Y. Wang, B. Staheli, Y. Katagiri, S. Cook, and R. Dai, “Design, modeling and control of a solar-powered quadcopter,” in *2018 IEEE International Conference on Robotics and Automation (ICRA)*, 2018, pp. 1251–1258.

[21] M. H. Shaheed, A. Abidali, J. Ahmed, S. Ahmed, I. Burba, P. J. Fani, G. Kwofie, K. Wojewoda, and A. Munjiza, “Flying by the sun only: The solarcopter prototype,” *Aerospace Science and Technology*, vol. 45, pp. 209–214, 2015. [Online]. Available: https://www.sciencedirect.com/science/article/pii/S1270963815001637

[22] A. Gong and D. Verstraete, “Fuel cell propulsion in small fixed-wing unmanned aerial vehicles: Current status and research needs,” *International Journal of Hydrogen Energy*, vol. 42, no. 33, pp. 21 311–21 333, 2017. [Online]. Available: https://www.sciencedirect.com/science/article/pii/S036031991732503X

[23] N. Lapeña-Rey, J. Blanco, E. Ferreyra, J. Lemus, S. Pereira, and E. Serrot, “A fuel cell powered unmanned aerial vehicle for low altitude surveillance missions,” *International Journal of Hydrogen Energy*, vol. 42, no. 10, pp. 6926–6940, 2017. [Online]. Available: https://www.sciencedirect.com/science/article/pii/S0360319917303038

[24] K. Swider-Lyons, R. Stroman, G. Page, M. Schuette, J. Mackrell, and J. Rodgers, “Hydrogen fule cell propulsion for long endurance small uvas,” in *AIAA Centennial of Naval Aviation Forum ”100 Years of Achievement and Progress”*. [Online]. Available: https://arc.aiaa.org/doi/abs/10.2514/6.2011-6975

[25] M. N. Boukoberine, M. F. Zia, M. Benbouzid, Z. Zhou, and T. Donateo, “Hybrid fuel cell powered drones energy management strategy improvement and hydrogen saving using real flight test data,” *Energy Conversion and Management*, vol. 236, p. 113987, 2021. [Online]. Available: https://www.sciencedirect.com/science/article/pii/S0196890421001631

[26] J. Apeland, D. Pavlou, and T. Hemmingsen, “State-of-technology and barriers for adoption of fuel cell powered multirotor drones,” in *2020 International Conference on Unmanned Aircraft Systems (ICUAS)*, 2020, pp. 1359–1367.

[27] “Our uav products.” [Online]. Available: https://www.intelligent-energy.com/our-products/uavs/

[28] W. J. Fredericks, M. D. Moore, and R. C. Busan, “Benefits of hybrid-electric propulsion to achieve 4x cruise efficiency for a vtol uav,” in *2013 International Powered Lift Conference*. [Online]. Available: https://arc.aiaa.org/doi/abs/10.2514/6.2013-4324

[29] M. N. Boukoberine, Z. Zhou, and M. Benbouzid, “A critical review on unmanned aerial vehicles power supply and energy management: Solutions, strategies, and prospects,” *Applied Energy*, vol. 255, p. 113823, 2019. [Online]. Available: https://www.sciencedirect.com/science/article/pii/S0306261919315107

[30] J. Hung and L. Gonzalez, “On parallel hybrid-electric propulsion system for unmanned aerial vehicles,” *Progress in Aerospace Sciences*, vol. 51, pp. 1–17, 2012. [Online]. Available: https://www.sciencedirect.com/science/article/pii/S0376042112000097

[31] W. Lu, D. Zhang, J. Zhang, T. Li, and T. Hu, “Design and implementation of a gasoline-electric hybrid propulsion system for a micro triple tilt-rotor vtol uav,” in *2017 6th Data Driven Control and Learning Systems (DDCLS)*, 2017, pp. 433–438.

[32] E. Cetinsoy, “Design and modeling of a gas-electric hybrid quad tilt-rotor uav with morphing wing,” in *2014 IEEE International Conference on Mechatronics and Automation*, 2014, pp. 1193–1198.

[33] T. Pang, K. Peng, F. Lin, and B. M. Chen, “Towards long-endurance flight: Design and implementation of a variable-pitch gasoline-engine quadrotor,” in *2016 12th IEEE International Conference on Control and Automation (ICCA)*, 2016, pp. 767–772.

[34] S. Sheng and C. Sun, “Control and optimization of a variable-pitch quadrotor with minimum power consumption,” *Energies*, vol. 9, no. 4, 2016. [Online]. Available: https://www.mdpi.com/1996-1073/9/4/232

[35] L. Gao, J. Zhao, Y. Zhu, H. Jin, H. Wang, and H. Cai, “Application of cycle variable pitch propeller to morphing unmanned aerial vehicles,” in *2015 IEEE International Conference on Information and Automation*, 2015, pp. 2493–2498.

[36] (2020, Sep) Long endurance heavy load hybrid drone uavs. [Online]. Available: https://www.uavfordrone.com/product/long-endurance-heavy-load-hybrid-drone-uavs/

[37] D. Pavković, M. Krznar, M. Cipek, D. Zorc, and M. Trstenjak, “Internal combustion engine control system design suitable for hybrid propulsion applications,” in *2020 International Conference on Unmanned Aircraft Systems (ICUAS)*, 2020, pp. 1614–1619.

[38] M. Krznar, D. Pavković, Y. Kozhushko, M. Cipek, D. Zorc, and M. Crneković, “Control system design for hybrid power supply of an unmanned aerial vehicle based on linearized averaged process models,” in *2020 International Conference on Unmanned Aircraft Systems (ICUAS)*, 2020, pp. 582–587.

[39] Y. Zhang, Z. Li, Y. Zhang, W. Xie, Z. Piao, and C. Hu, “Performance improvement of direct power control of pwm rectifier with simple calculation,” *IEEE Transactions on Power Electronics*, vol. 28, no. 7, pp. 3428–3437, 2013.

[40] Z. Yin, J. Liu, and Y. Zhong, “Study and control of three-phase pwm rectifier based on dual single-input single-output model,” *IEEE Transactions on Industrial Informatics*, vol. 9, no. 2, pp. 1064–1073, 2013.

[41] J. Espinoza, G. Joos, and L. Moran, “Decoupled control of the active and reactive power in three-phase pwm rectifiers based on non-linear control strategies,” in *30th Annual IEEE Power Electronics Specialists Conference. Record. (Cat. No.99CH36321)*, vol. 1, 1999, pp. 131–136 enervol.1.

[42] J. W. Dixon and Boon-Teck Ooi, “Indirect current control of a unity power factor sinusoidal current boost type three-phase rectifier,” *IEEE Transactions on Industrial Electronics*, vol. 35, no. 4, pp. 508–515, 1988.

[43] E. M. Thajeel, M. M. Mahdi, and E. I. Abbas, “Fuzzy logic controller based shunt active power filter for current harmonic compensation,” in *2020 International Conference on Computer Science and Software Engineering (CSASE)*, 2020, pp. 94–99.

[44] S. N. Manias, “4 - diode rectifiers,” in *Power Electronics and Motor Drive Systems*. Academic Press, 2017, pp. 111–181.

[45] S.N.Manias, “Pwm or switched mode rectifiers,” in *Power Electronics and Motor Drive Systems*. Academic Press, 2017, pp. 657–694.

[46] Q. Zhong and G. C. Konstantopoulos, “Current-limiting three-phase rectifiers,” *IEEE Transactions on Industrial Electronics*, vol. 65, no. 2, pp. 957–967, 2018.

[47] S. Bayhan and H. Komurcugil, “Sliding-mode control strategy for three-phase three-level t-type rectifiers with dc capacitor voltage balancing,” *IEEE Access*, vol. 8, pp. 64 555–64 564, 2020.

[48] H. Guo, H. Wang, and S. Lin, “Robust sliding mode control of three-phase four-switch pwm voltage-source rectifier with uncertainties and disturbances,” in *2018 13th IEEE Conference on Industrial Electronics and Applications (ICIEA)*, 2018, pp. 486–490.

[49] M. A. Fnaiech, M. Trabelsi, S. Khalil, M. Mansouri, H. Nounou, and H. Abu-Rub, “Robust sliding mode control for three-phase rectifier supplied by non-ideal voltage,” *Control Engineering Practice*, vol. 77, pp. 73–85, 2018.

[50] X.Feng, Y.Tao, X.Cui, K.Shao, and Y.Wang, “Sliding mode and predictive current control strategy of the three-phase vienna rectifier,” *Journal of Power Electronics*, vol. 20, no. 3, pp. 743–753, 2020.

[51] J. A. Cortajarena, O. Barambones, P. Alkorta, and J. Cortajarena, “Sliding mode control of an active power filter with photovoltaic maximum power tracking,” *International Journal of Electrical Power & Energy Systems*, vol. 110, pp. 747 – 758, 2019.

[52] R.-J. Wai and Y. Yang, “Design of backstepping direct power control for three-phase pwm rectifier,” *IEEE Transactions on Industry Applications*, vol. 55, no. 3, pp. 3160–3173, 2019.

[53] Y. Jiang, J. Wang, Q. Li, Y. Feng, and X. Mu, “The passivity-based hybrid control of npc hybrid three phase voltage source rectifier,” in *2018 IEEE International Power Electronics and Application Conference and Exposition (PEAC)*, 2018, pp. 1–6.

[54] H. Komurcugil and S. Bayhan, “Passivity-based control strategy for single-phase three-level t-type pwm rectifiers,” in *2020 IEEE 29th International Symposium on Industrial Electronics (ISIE)*, 2020, pp. 1179–1184.

[55] D. N. S., G. Nadh, and A. R. S., “A novel predictive control for an active front end rectifier using lyapunov stability criteria,” in *IECON 2019 - 45th Annual Conference of the IEEE Industrial Electronics Society*, vol. 1, 2019, pp. 1532–1537.

[56] G. C. Konstantopoulos and A. T. Alexandridis, “Design and analysis of a novel bounded nonlinear controller for three-phase ac/dc converters,” in *52nd IEEE Conference on Decision and Control*, 2013, pp. 3659–3664.

[57] K. F. Krommydas and A. T. Alexandridis, “Nonlinear stability analysis for ac/dc voltage source converters driven by pi current-mode controllers,” in *2014 European Control Conference (ECC)*, 2014, pp. 2774–2779.

[58] M. Kissaoui, A. Al Tahir, A. Abouloifa, F. Chaoui, Y. Abouelmahjoub, and F. Giri, “Output-feedback nonlinear adaptive control strategy of three-phase ac/dc boost power converter for on-line ups systems,” *IFAC-PapersOnLine*, vol. 49, no. 13, pp. 324–329, 2016, 12th IFAC Workshop on Adaptation and Learning in Control and Signal Processing ALCOSP 2016.

[59] J. Benzaquen and B. Mirafzal, “Seamless dynamics for wild-frequency active rectifiers in more electric aircraft,” *IEEE Transactions on Industrial Electronics*, vol. 67, no. 9, pp. 7135–7145, 2020.

[60] Y. Yin, J. Liu, W. Luo, L. Wu, S. Vazquez, J. I. Leon, and L. G. Franquelo, “Adaptive control for three-phase power converters with disturbance rejection performance,” *IEEE Transactions on Systems, Man, and Cybernetics: Systems*, vol. 51, no. 2, pp. 674–685, 2021.

[61] Y. Yin, J. Liu, W. Luo, L. Wu, S. Vazquez, J. I. Leon, and L. G. Franquelo, “Adaptive control for three-phase power converters with disturbance rejection performance,” *IEEE Transactions on Systems, Man, and Cybernetics: Systems*, vol. 51, no. 2, pp. 674–685, 2021.

[62] A. Hadri-Hamida, A. Allag, M. Hammoudi, S. Mimoune, S. Zerouali, M. Ayad, M. Becherif, E. Miliani, and A. Miraoui, “A nonlinear adaptive backstepping approach applied to a three phase pwm ac–dc converter feeding induction heating,” *Communications in Nonlinear Science and Numerical Simulation*, vol. 14, no. 4, pp. 1515–1525, 2009.

[63] B. K. Bose, *Modern power electronics and AC drives*. Prentice Hall PTR, 2002.

[64] D. Mondal, A. Chakrabarti, and A. SenGupta, *Power System Small Signal Stability Analysis and Control*. Academic Press; 2nd ed, 2020.

[65] H. Komurcugil and O. Kukrer, “Lyapunov-based control for three-phase pwm ac/dc voltage-source converters,” *IEEE Transactions on Power Electronics*, vol. 13, no. 5, pp. 801–813, 1998.

[66] V. M. Popov, *Hyperstability of control systems*. Springer-Verlag, 1973.

[67] D. Rathnakumar, J. LakshmanaPerumal, and T. Srinivasan, “A new software implementation of space vector pwm,” in *Proceedings. IEEE SoutheastCon, 2005.*, 2005, pp. 131–136.

[68] J. Rodriguez, J. Dixon, J. Espinoza, J. Pontt, and P. Lezana, “Pwm regenerative rectifiers: state of the art,” *IEEE Transactions on Industrial Electronics*, vol. 52, no. 1, pp. 13–15, 2005.

[69] J. R. Rodriguez, J. W. Dixon, J. R. Espinoza, J. Pontt, and P. Lezana, “Pwm regenerative rectifiers: state of the art,” *IEEE Transactions on Industrial Electronics*, vol. 52, no. 1, pp. 5–22, 2005.